Article

Cell Reports

Active Zone Scaffold Protein Ratios Tune Functional Diversity across Brain Synapses

Graphical Abstract

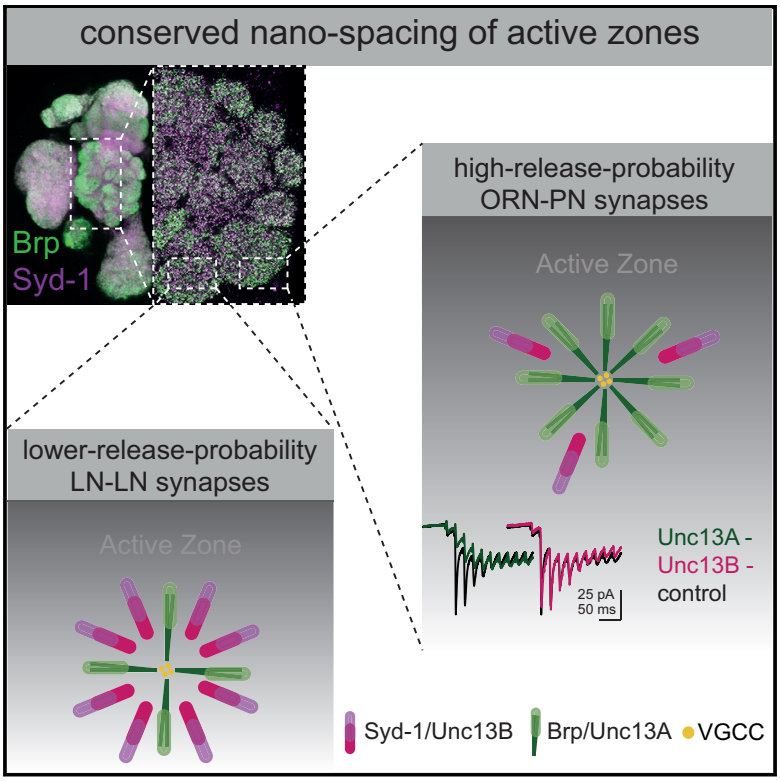

Highlights

- Active zone scaffold proteins systematically differ between synapse types in *Drosophila*
- BRP localizes Unc13A 30–40 nm closer to voltage-gated Ca^{2+} channels than Syd-1 Unc13B
- BRP/Unc13A dominates at fast, depressing, Syd-1/Unc13B at slow, facilitating synapses

Authors

Andreas Fulterer, Till F.M. Andlauer, Anatoli Ender, ..., Alexander M. Walter, Katherine I. Nagel, Stephan J. Sigrist

Correspondence

katherine.nagel@nyumc.org (K.I.N.), stephan.sigrist@fu-berlin.de (S.J.S.)

In Brief

Fulterer et al. demonstrates that the scaffold proteins Bruchpilot and Syd-1 cluster (M)Unc13 release factor isoforms either close (BRP/Unc13A) or further away (Syd-1/Unc13B) from voltage-gated Ca^{2+} channels in the *Drosophila* olfactory system. These scaffold/release factor "modules" varied significantly between different synapse types, thereby tuning release features toward depression or facilitation.

Fulterer et al., 2018, Cell Reports *23*, 1259–1274
May 1, 2018
https://doi.org/10.1016/j.celrep.2018.03.126

CellPress

Cell Reports
Article

Active Zone Scaffold Protein Ratios Tune Functional Diversity across Brain Synapses

Andreas Fulterer,[1,9] Till F.M. Andlauer,[2,3,9] Anatoli Ender,[4,9] Marta Maglione,[1,5,6,9] Katherine Eyring,[8] Jennifer Woitkuhn,[1] Martin Lehmann,[6] Tanja Matkovic-Rachid,[1] Joerg R.P. Geiger,[5,7,10] Alexander M. Walter,[6,10] Katherine I. Nagel,[8,10,*] and Stephan J. Sigrist[1,5,10,11,*]

[1]Institute for Biology/Genetics, Freie Universität Berlin, 14195 Berlin, Germany
[2]Max Planck Institute of Psychiatry, 80804 Munich, Germany
[3]Department of Neurology, Klinikum rechts der Isar, Technical University of Munich, 81675 Munich, Germany
[4]German Center for Neurodegenerative Disorders, Charité Universitätsmedizin Berlin, 10117 Berlin, Germany
[5]NeuroCure Cluster of Excellence, Charité Universitätsmedizin, 10117 Berlin, Germany
[6]Leibniz-Forschungsinstitut für Molekulare Pharmakologie (FMP), 13125 Berlin, Germany
[7]Institut für Neurophysiologie, Charité Universitätsmedizin, 10117 Berlin, Germany
[8]Neuroscience Institute, NYU School of Medicine, New York, NY 10016, USA
[9]These authors contributed equally
[10]Senior author
[11]Lead Contact
*Correspondence: katherine.nagel@nyumc.org (K.I.N.), stephan.sigrist@fu-berlin.de (S.J.S.)
https://doi.org/10.1016/j.celrep.2018.03.126

SUMMARY

High-throughput electron microscopy has started to reveal synaptic connectivity maps of single circuits and whole brain regions, for example, in the *Drosophila* olfactory system. However, efficacy, timing, and frequency tuning of synaptic vesicle release are also highly diversified across brain synapses. These features critically depend on the nanometer-scale coupling distance between voltage-gated Ca^{2+} channels (VGCCs) and the synaptic vesicle release machinery. Combining light super resolution microscopy with *in vivo* electrophysiology, we show here that two orthogonal scaffold proteins (ELKS family Bruchpilot, BRP, and Syd-1) cluster-specific (M)Unc13 release factor isoforms either close (BRP/Unc13A) or further away (Syd-1/Unc13B) from VGCCs across synapses of the *Drosophila* olfactory system, resulting in different synapse-characteristic forms of short-term plasticity. Moreover, BRP/Unc13A versus Syd-1/Unc13B ratios were different between synapse types. Thus, variation in tightly versus loosely coupled scaffold protein/(M)Unc13 modules can tune synapse-type-specific release features, and "nanoscopic molecular fingerprints" might identify synapses with specific temporal features.

INTRODUCTION

Synapses are highly specialized structures responsible for the flow of information between neurons. Synapses can exhibit high or low release probabilities. Different release probabilities often distinguish synapses of distinct neuronal populations and account for the diversity of synapse response time (fast and slow synapses), signal strength, and the adaption to signal trains (short-term plasticity) (Gjorgjieva et al., 2016; Jackman and Regehr, 2017). Biophysical and electrophysiological analyses have suggested that both release probability and short-term plasticity depend greatly on the nanometer-scale distance (coupling distance) between synaptic vesicles (SVs) with their Ca^{2+} sensor Synaptotagmin, and the voltage-operated Ca^{2+} channels (VGCCs). VGCCs mediate Ca^{2+} influx in response to membrane depolarizations caused by action potentials (Eggermann et al., 2011; Stanley, 2016; Vyleta and Jonas, 2014; Wadel et al., 2007; Wang et al., 2016). Essential release factors of the (M)Unc13 protein family thereby seem to define SV release sites and position SVs relative to the VGCCs (Böhme et al., 2016; Sakamoto et al., 2018).

Effective coupling distances vary across mammalian brain synapses, resulting in major functional differences (Eggermann et al., 2011). The molecular mechanisms and proteins controlling these coupling distances remained rather enigmatic for a long time. Notably, only a few conserved families of large scaffold proteins organize the presynaptic active zone (AZ), giving AZs their typical ultrastructural shape and conferring stability to release sites (Petzoldt et al., 2016; Südhof, 2012). The AZ scaffold proteins in both rodents and *Drosophila* cluster Ca^{2+} channels and release factors, particularly (M)Unc13 which is essential for SV release (Böhme et al., 2016; Wang et al., 2016). Consequently, these molecules are crucial for patterning evoked SV release.

The functional diversity of specific synapses ultimately must be encoded within their molecular makeup, and molecular diversity exists even within traditional neurotransmitter type classifications (O'Rourke et al., 2012). However, whether molecular "design principles" exist that tune functional diversity over a spectrum of synapse types, remain relevant, but unresolved questions.

We show here that the ratio between two AZ scaffold proteins (ELKS family Bruchpilot [BRP] and Syd-1) varies widely across synapse types of the *Drosophila* brain and thereby tunes their effective coupling distance. BRP was responsible for clustering the (M)Unc13 release factor isoform Unc13A close to the

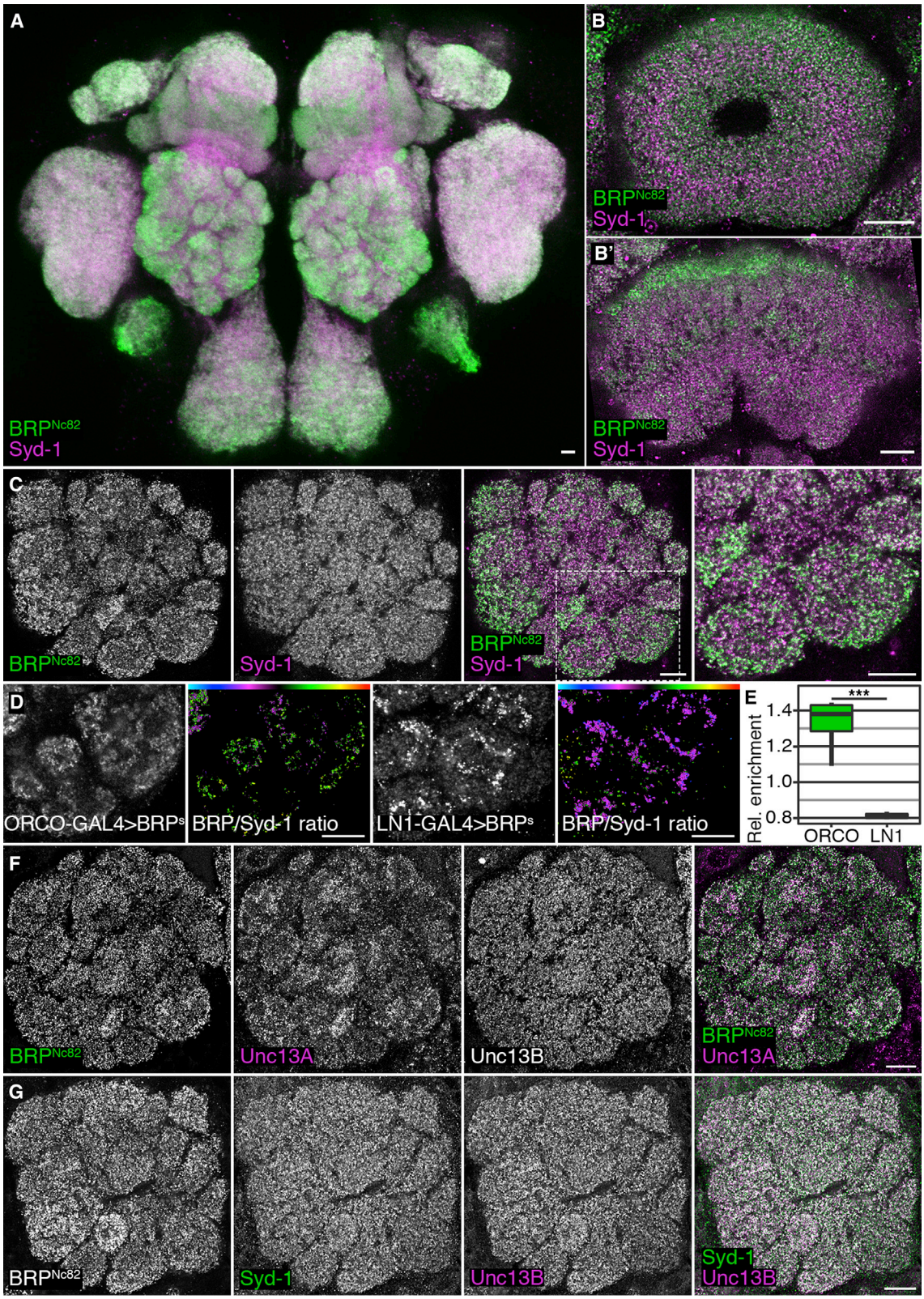

(legend on next page)

VGCCs (≈70 nm), while Syd-1 clustered Unc13B further away (> 100 nm). High BRP/Unc13A levels promoted a high release probability at the first relay synapse of the olfactory system and, consequently, supported a fast but depressing release component. By contrast, neighboring interneuron synapses and the second relay projection neuron synapse expressed low Unc13A levels and depended more strongly on Unc13B. Varying tightly versus loosely coupled scaffold protein/(M)Unc13 complexes at presynaptic AZs might, thus, be a principle for tuning synaptic release features. AZ scaffold proteins therefore operate close to the top of an epistatic molecular hierarchy diversifying the release features of synapse types via a differential positioning of Unc13 isoforms.

RESULTS

AZ Scaffold Composition Diversity across *Drosophila* Brain Synapses

We started by asking whether variation in presynaptic AZ scaffold architecture might contribute to synapse diversity, and stained adult *Drosophila* brains for two major organizing scaffold proteins: BRP, a key component of the T-bar organization within the AZ center (Kittel et al., 2006), and Syd-1, a conserved AZ protein (Wentzel et al., 2013) localized at the edge of the AZ nanoarchitecture (Owald et al., 2010).

While both scaffold proteins were expressed in all synaptic areas of the brain (not shown), the relative intensity of Syd-1 and BRP varied between CNS regions and within them (Figure 1A). For example, the central brain ellipsoid (Figure 1B) and fan-shaped bodies (Figure 1B′), higher integrative centers for control of locomotion, showed differential staining patterns between the two scaffold proteins. These patterns were observed robustly across experiments and were present both in immunostainings using different antibodies (e.g., various antibodies against BRP), and in the fluorescence signals of GFP knock-in lines (not shown). Thus, these patterns are not artifacts caused by fixation or penetration differences, but instead, reflect real differences in the molecular composition between AZs belonging to distinct synapse types.

AZ Scaffold Composition Predicts Unc13 Isoform Diversity in the Olfactory System

The *Drosophila* olfactory system is an important model for studying synaptic principles of sensory information processing, routing, and encoding (Wilson, 2013). Olfactory receptor neurons (ORNs) in the antennal lobe (AL) convey olfactory information from the antenna onto projection neurons (PNs), which carry the information processed within the AL circuit to higher brain centers, called the lateral horn (LH) and mushroom body (MB). Information processing is tuned by local interneurons (LNs) (Chou et al., 2010; Nagel et al., 2015). BRP levels in the AL were high at the cortex of individual AL glomeruli (Figure 1C, see magnified image to the right), a position typical for ORN terminals (Mosca and Luo, 2014; Rybak et al., 2016). Syd-1, however, was distributed rather homogeneously over individual glomeruli and the whole AL. We expressed the AZ scaffold marker BRP-short-GFP (Schmid et al., 2008) within the principal AL neuron populations to test directly to which neuron type these BRP-rich presynaptic AZs belong. Note that BRP-short integrates into AZ scaffolds, but does not contain the C-terminal BRP epitope recognized by the antibody used for our BRP immunostaining (Kremer et al., 2010). When using an ORN-specific driver line (ORCO-GAL4), the BRP expression pattern followed the distribution of ORN-derived AZs (Figure 1D), and BRP/Syd-1 ratios were high in ORN-derived AZs (Figures 1D, second image, and 1E). By contrast, when using the interneuron-specific LN1-GAL4 line, GFP was expressed primarily toward the center of individual glomeruli, and BRP/Syd-1 ratios were low at interneuron-derived AZs (Figures 1D, fourth image, and 1E). BRP is, thus, highly expressed at ORN-derived AZs, but less highly at interneuron-derived AZs.

We have shown previously that expression of BRP-short does not influence AZ number, AZ density, or the terminal area in the MB calyx of adult *Drosophila* (Kremer et al., 2010). Nevertheless we wanted to rule out that the observed differences in BRP/Syd-1 levels across AL AZ populations might have been influenced by expression of *brp-short* constructs. We therefore compared BRP/Syd-1 ratios in neuronal populations expressing either BRP-short-GFP or membrane-associated GFP (mCD8-GFP). Neither average BRP and Syd-1 intensities nor the BRP/Syd-1 ratio changed significantly between BRP-short-GFP- and mCD8-GFP-expressing animals (Figure S1A). The differences in BRP/Syd-1 ratios observed using BRP-short-GFP could be replicated when using mCD8-GFP (Figure S1B).

BRP and Syd-1 operate as "molecular spacers" at peripheral neuromuscular junction (NMJ) synapses of *Drosophila* larvae, and they define Ca^{2+} channel coupling distances via differential positioning of either the Unc13 isoform Unc13A (via BRP, more closely coupled) or Unc13B (via Syd-1, more loosely coupled) (Böhme et al., 2016). Thus, we tested whether AZs were

Figure 1. Distribution of Scaffold Proteins Syd-1 and Brp and Release Factor Unc13 Isoforms A and B in Different Neuron Populations of Adult *Drosophila melanogaster* Brains

(A–C) Confocal images of adult *Drosophila* w^{1118} brains stained against Syd-1 (magenta) and BRP^{Nc82} (green). All scale bars, 10 μm. Central brain maximum intensity projection of a confocal stack (A). Ellipsoid body (B). Fan-shaped body (B′). (C) Antennal lobe (AL), the blow-up shows AL glomeruli VA2 and VA3 (C).

(D) False color-coded median BRP/Syd-1 ratio in the AL glomeruli VA2 and VA3. The AZs of ORNs were highlighted using BRP-short-GFP (BRP^{S}) expressed by ORCO-GAL4 and AZs of inhibitory LNs using LN1-GAL4. Color gradients visualize the ratio between Syd-1 and BRP^{Nc82} (high BRP/Syd-1: green-red; low BRP/Syd-1: magenta-cyan).

(E) GFP-positive median ratios were normalized by median ratios of the surrounding AL to illustrate the relative difference between GFP-positive AZs and the surrounding AL. The AZs positive for ORCO-GAL4 > BRP^{S} were enriched for BRP in comparison to LN1-derived AZs; Mann-Whitney U (MWU) test result: $p = 0.000155$, $n = 8$ each. The graph shows medians, interquartile ranges, and min/max values.

(F) AL stained against BRP^{Nc82} (green), Unc13A (magenta), and Unc13B.

(G) AL stained against BRP^{Nc82}, Syd-1 (green), and Unc13B (magenta).

See also Figures S1, S2, and S6.

differentially associated with the release factor Unc13 isoforms A and B within the AL. Unc13A matched BRP expression closely throughout the AL (Figure 1F). As BRP is highly expressed at ORN-derived AZs (Figures 1D and 1E), we conclude that Unc13A is also enriched at ORN-derived AZs (see also Figures 5A and 5B) and confirmed this observation using Spearman correlation-based colocalization analysis (Figure S2A). Unc13B and Syd-1 colocalized as well but were distributed more homogeneously over AL AZs (Figure 1G). Notably, the ORN-to-PN synapse is characterized by a high release probability (Kazama and Wilson, 2008), while LN synapses onto both ORNs and other LNs are rather slow and facilitating (Liu and Wilson, 2013; Nagel et al., 2015; Nagel and Wilson, 2016). Thus, the distribution of Unc13 isoforms and their associated central (BRP/Unc13A) and peripheral (Syd-1/Unc13B) scaffolding proteins correlates with the known properties of AL synapses.

The PN boutons synapse onto MB Kenyon cell (KC) dendrites form so-called PN microglomeruli in the MB calyx (Kremer et al., 2010), the second relay of the olfactory system. These synapses operate slowly and need to adapt to the very high action potential (AP) frequencies typical for PNs (above 100 Hz) (Gruntman and Turner, 2013). The AZs derived from either KCs or LNs are positioned in between the microglomeruli (Christiansen et al., 2011). The BRP staining showed a rather homogeneous distribution over the calyx (Figure 2A). By contrast, Syd-1 labeling was very strong within microglomeruli (Figure 2A, yellow circles and arrows), where PN boutons synapse onto KC dendrites. We quantified BRP/Syd-1 ratios expressing BRP-short with PN- and KC-specific (Figure 2B) driver lines. The AZs of PNs were strongly enriched for Syd-1 (Figure 2C). Next, we compared Unc13A and Unc13B staining to BRP and Syd-1 (Figures 2D and 2E). As in the AL, the Unc13A distribution matched the BRP distribution (Figure 2D). Similarly, Unc13B strictly followed the Syd-1 pattern (Figure 2E), as confirmed by colocalization analysis (Figure S2B). Unc13B, thus, accumulated at the AZs of PN boutons and was only weakly expressed at the AZs outside microglomeruli (see the magnified image in Figure 2E).

Thus, these two relays of the olfactory system feature an antagonistic expression pattern of Unc13 isoforms: Unc13A enriched in ORN-derived AZs while Unc13B enriched in PN-derived AZs within the calyx. At the same time, the scaffold protein BRP is enriched at ORN- and Syd-1 at PN-derived AZs. Each of these distribution patterns is consistent with the known dynamics of particular synapses, with ORN-to-PN synapses supporting fast transmission, and PN-to-KC synapses exhibiting slow transmission.

BRP Specifically Recruits Unc13A while Syd-1 Specifically Recruits Unc13B to AZs in the *Drosophila* Brain

We next analyzed whether BRP and Syd-1 recruit specific Unc13 isoforms to AZs. Knockdown (KD) of *brp* using RNAi constructs with a pan-neuronal driver line (elav-GAL4) drastically reduced Unc13A levels within the AL (Figures 3A and 3C), while Unc13B levels were not reduced (Figure 3C, left). Knockout of *syd-1* (Figure S3) reduced Unc13B levels specifically (Figures 3B and 3C, middle). Thus, BRP and Syd-1 not only colocalize with Unc13A and B, respectively, but are necessary for their localization to specific AZs in a largely uncoupled, orthogonal manner. Notably, this relation was unidirectional: the scaffold proteins controlled Unc13 isoform AZ recruitment, but not vice versa. Elimination of either Unc13A or Unc13B had no major consequences on the levels or distribution of either scaffold protein (Figure 3C, right).

We also conducted the same analysis in the MB calyx. As expected, Unc13A clustering was strongly affected by *brp* KD, but not by the elimination of Syd-1 (Figures 3D–3F), while the Unc13B localization was specifically impeded in *syd-1* mutants (Figures 3E and 3F, right). Unc13B staining levels were higher in the PN boutons of *brp* KD animals than in the controls (Figure 3F, left). Thus, BRP clusters Unc13A and Syd-1 clusters Unc13B across several synapse types of the *Drosophila* olfactory system. This mechanism likely extends over the whole brain (not shown).

Super Resolution at ORN-to-PN Synapses: Unc13A Is Closer to Ca^{2+} Channels Than Unc13B

At NMJ synapses, Unc13A clusters more closely to Ca^{2+} channels than Unc13B, conferring a high release probability to individual APs (Böhme et al., 2016). To examine whether the same clustering principle applies to central cholinergic synapses, we analyzed the nanoscopic pattern of the AZ scaffold at the ORN output synapses with stimulated emission depletion (STED) microscopy. Using this technique (Kittel et al., 2016), we examined whether—similar to NMJ synapses—Unc13A localizes more closely to AZ centers than Unc13B at central ORN-derived AZs.

Due to the rather superficial position of the AL synapses (Spühler et al., 2016), STED imaging with a high resolution of 50 nm (instead of 250 nm achievable in confocal scans) was possible in the AL (Figure 4A). BRP-short-GFP was expressed in ORNs and imaged in parallel to the STED channels to identify ORN-derived AZs (Figure 4A, blue label). The ORN-derived synapses form elongated AZs, at which multiple T bars are fused and arranged opposite to multiple postsynaptic profiles ("dyad synapses") (Mosca and Luo, 2014; Rybak et al., 2016). Elongated BRP staining patterns were thus expected, as BRP is the major building block of T bars. The BRP C terminus, labeled by the Nc82 monoclonal antibody, maps to the distal part ("roof") of T bars at NMJ synapses (Fouquet et al., 2009). Planar views of T bars show a ring-like distribution of BRP Nc82 epitopes (Fouquet et al., 2009; Mosca and Luo, 2014). By contrast, the BRP N terminus labels the pedestal ("foot") structure of the T bar above Ca^{2+} channels at the center of the AZ. Accordingly, multiple T bars nearby should thus be visible as an extended rod-like BRP C-term label with periodic foci of BRP N-term signal. This was indeed observed: the BRP short-labeled ORN-derived AZs featured extended BRP signals with multiple BRP N-term foci (Figures 4A and 4D). Depending on the angle of imaging, BRP C-term signals (Nc82) appeared as either elongated rod-like structures or concatenated ring structures (Figure 4A, upper and lower image, respectively; see Figure 4D for a schematic representation). BRP formed simple rings in between the clusters of the elongated ORN-derived AZs, where interneuron synapses are located (not shown). We investigated the nano-spacing of Unc13 isoforms at ORN output AZs, concentrating on planar-imaged AZs appearing as rings (Figures 4B and 4C,

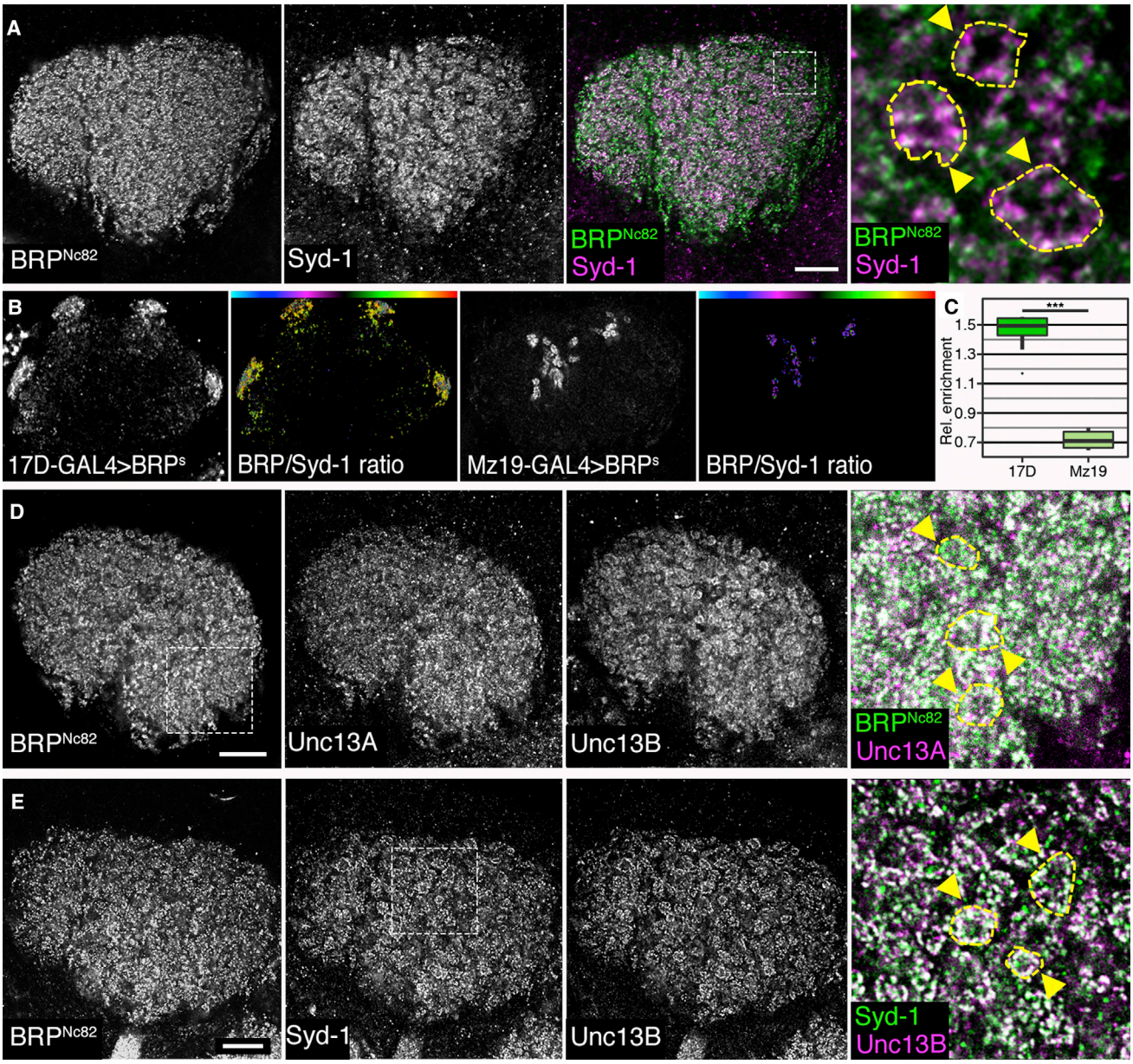

Figure 2. Distribution of Scaffold Proteins Syd-1 and BRP and the Unc13 Isoforms A and B in the Mushroom Body Calyx of Adult *Drosophila*

Confocal images of adult *Drosophila* w^{1118} mushroom body calyces. All scale bars, 10 μm.

(A) Staining against BRP^{Nc82} (green) and Syd-1 (magenta); the blow-up highlights microglomerular structures labeled by yellow dashed lines and arrowheads.

(B) False color-coded median BRP/Syd-1 ratio in calyces. The AZs of KCs were highlighted using BRP-short-GFP (BRP^{S}) expressed by 17D-GAL4 and AZs of PNs using Mz19-GAL4. Color gradients visualize the ratio between Syd-1 and BRP^{Nc82}.

(C) GFP-positive median ratios were normalized by median ratios of the surrounding calyx. The AZs positive for 17D-GAL4 > BRP^{S} were enriched for BRP in comparison to Mz19-derived AZs; MWU test result: p = 0.00000983, n = 8 for 17D and n = 13 for Mz19.

(D) Calyx stained against BRP^{Nc82} (green), Unc13A (magenta), and Unc13B, blow-up highlights microglomeruli outlined by yellow dashed lines and arrowheads.

(E) Calyx stained against BRP^{Nc82}, Syd-1 (green), and Unc13B (magenta), blow-up shows microglomeruli indicated by yellow dashed lines and arrowheads.

Graphs as explained for Figure 1.

See also Figure S2.

planar images). Unc13A colocalized tightly with the BRP C-term signals, while Unc13B was located at greater distances.

The BRP C-term signal surrounds Ca^{2+} channels at the center of AZs at NMJ synapses, while Syd-1 localizes more toward the AZ edge (Owald et al., 2010). Quantification of STED data at these peripheral synapses revealed an average distance of 120 nm between Unc13B and GFP-labeled Ca^{2+} channels (the voltage-gated α1 subunit *Cacophony* expressed using the

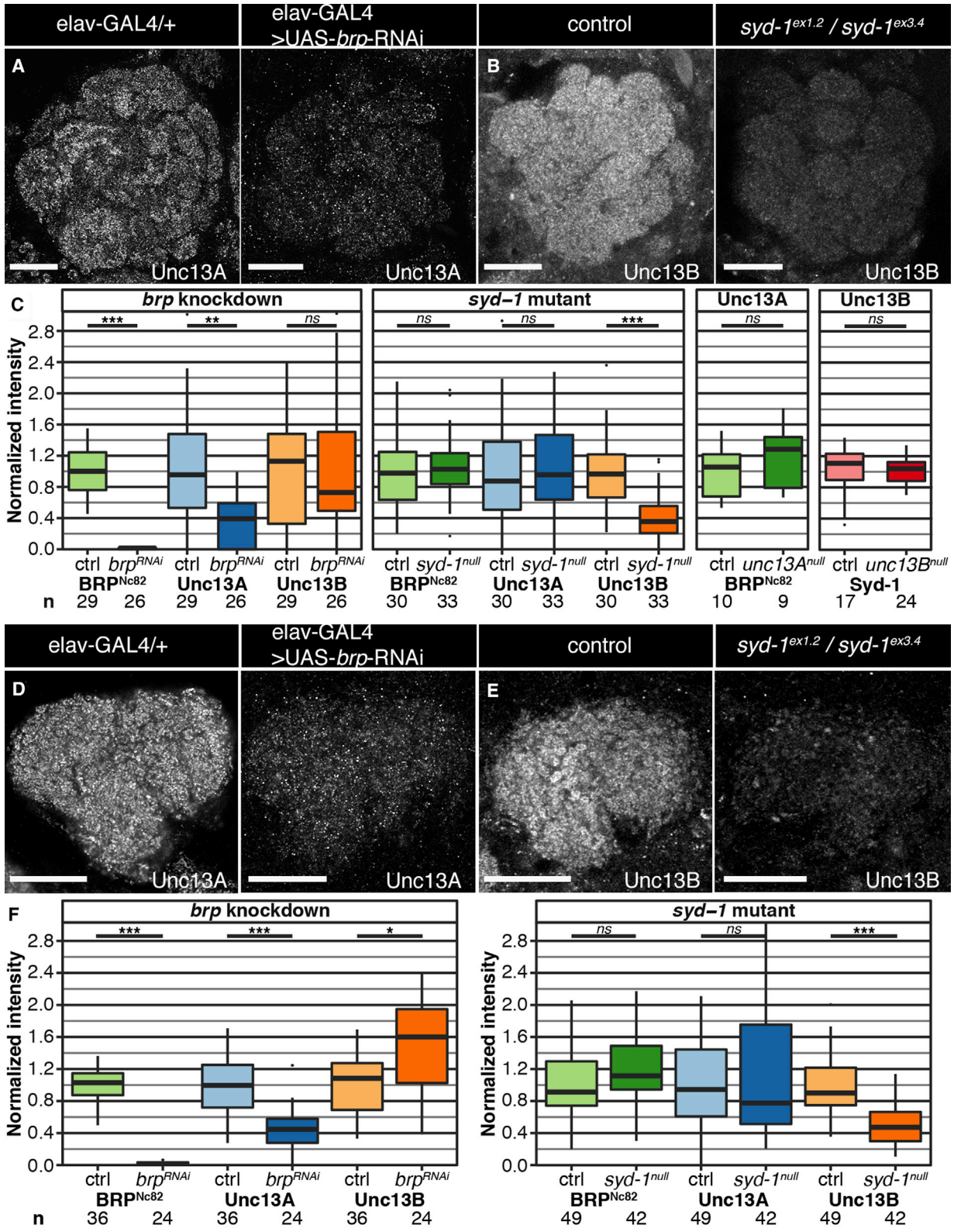

(legend on next page)

GAL4 system, Cac-GFP), while Unc13A was positioned only 70 nm away (Böhme et al., 2016). To test whether similar differences in coupling distances might exist at ORN-derived AZs, we expressed Cac-GFP within ORNs and co-stained brains with either Unc13A (Figure 4E) or Unc13B (Figure 4F) to quantify the coupling distances (Figures 4G and 4H). A higher overlap between Cac-GFP and Unc13A than with Unc13B was already discernable at low magnification (compare overlap given by the white signal in Figures 4E and 4F, left images). Cac-GFP formed discrete dots at STED resolution, corresponding to the center of single BRP rings at a position approximately at the AZ center. Unc13A localized significantly closer to Cac-GFP dots than Unc13B (compare the planar image in Figures 4E with 4F), as confirmed by quantification (Figure 4H). Distances were very similar to the ones at NMJ synapses (Böhme et al., 2016). Thus, the sub-AZ nanospacing is similarly organized at the cholinergic ORN output synapses, as it is at glutamatergic NMJs: a cluster of Ca^{2+} channels at the center of the AZ localizes beneath an elongated stretch of BRP proteins, which is surrounded by discrete Unc13A and Unc13B clusters at distinct distances. We next asked whether the two Unc13 isoforms support different release components.

Unc13A Steers Fast, Phasic Release and Plasticity at ORN-to-PN Synapses

To test the functional role of each Unc13 isoform at a central synapse, we generated transgenic RNAi lines that specifically reduced Unc13A and Unc13B levels. When expressed only in ORNs (pan-ORN driver pb-GAL4), *unc13A* RNAi eliminated nearly all the Unc13A label within the AL (Figure 5A). This indicates that most of the Unc13A in the AL is localized at ORN output AZs, in line with our finding that Unc13A is strongly enriched at ORN output synapses (Figures 1F and S2A). The Unc13B label was not altered by ORN-specific KD of Unc13A (Figure 5A). ORN-driven RNAi against *unc13B* generated holes in the Unc13B AL staining (Figure 5B), at the positions typical for ORN synapses (at the cortex of glomeruli). However, substantial label remained, consistent with our finding that Unc13B is rather homogeneously distributed across AL synapse populations. Thus, neurons other than ORNs, particularly interneurons, contribute to the Unc13B label in the AL.

To test the role of each isoform in ORN-PN synaptic transmission, we expressed either the *unc13A* or *unc13B* RNAi in ORNs and recorded synaptic currents from postsynaptic PN neurons while electrically stimulating the antennal nerve, which contains ORN axonal fibers. The antennal nerve was stimulated at 10 Hz and then 50 Hz to simulate spontaneous and odor-evoked firing rates, respectively (Kazama and Wilson, 2008; Nagel et al., 2015). Postsynaptic PNs were identified by their characteristic location and size. The PN input resistances, which have been shown to correlate with EPSC size (Kazama and Wilson, 2008), were similar across control and KD flies (600–1,200 MΩ, Figure S4A). The stimulation current (10–100 μA) was gradually increased until a reliable EPSC was evoked. Recordings in which the stimulation current was >100 μA were excluded.

Synaptic transmission at the ORN-PN synapse is typically fast and depresses with repeated stimulation (Figures 5C, 5D, and 5F) (Kazama and Wilson, 2009; Nagel et al., 2015). However, RNAi-mediated KD of *unc13A* reduced the amplitude of single EPSCs (Figures 5C–5E) and produced synaptic facilitation in response to a 10 Hz train of stimuli, both of which suggest a reduction in release probability (Figures 5C, 5D, and 5F). Of note, significantly larger currents were required to elicit EPSCs in these flies (Figure S4B). Increasing the stimulation frequency from 10 to 50 Hz in control flies evokes fast EPSCs with renewed depression (Figures 5C, 5D, and 5F). These fast EPSCs were absent or reduced in *unc13A* KD flies, resulting in a significantly longer latency to peak current (Figure 5G). A very similar phenotype was observed in flies overexpressing an N-terminal fragment of Unc13A (Figure S5), which lacks the catalytic MUN domain, in ORNs. We have previously shown that this fragment displays a dominant-negative phenotype at NMJ synapses (Reddy-Alla et al., 2017). These data provide independent evidence that Unc13A promotes a fast, transient component of SV release at the ORN-to-PN synapse.

In clear contrast to the loss of *unc13A*, KD of *unc13B* spared fast ORN-PN transmission (Figures 5A–5E). Here, paired-pulse dynamics and the latency to peak response during 50-Hz stimulation were not significantly different from control recordings. Moreover, a fast component was observed in all recordings during 50-Hz stimulation. These data are consistent with a model in which Unc13B is dispensable for fast synaptic transmission.

Taken together, Unc13A is of specific importance for fast release at this synapse. The data strongly imply that the BRP-mediated positioning of Unc13A close to Ca^{2+} channels promotes the high release probability typical for this synapse.

Figure 3. Reduction of Scaffold Proteins BRP and Syd-1 Results in Isoform-Specific Downregulation of Unc13s in the Adult *Drosophila* Brain

(A and B) Confocal images of ALs stained against BRP^{Nc82}, Unc13A, and Unc13B. All scale bars, 20 μm. Flies with a pan-neuronal *brp* knockdown (KD; *elav-GAL4 > UAS-brp-RNAi*) in comparison to a control group (elav-GAL4/+); staining against Unc13A (A). *syd-1*^{null} mutant flies ($syd^{ex1.2}/syd^{ex3.4}$) in comparison to w^{1118} controls; staining against Unc13B (B).

(C) Average staining intensities of BRP, Unc13A, and Unc13B in the KD or deletion situation normalized to controls show a significant downregulation of average intensity levels of Unc13A ($p = 0.0016$ for the *brp* KD). Syd-1 deletion results in downregulation of Unc13B ($p = 0.000008$). Average intensities of BRP and Syd-1 in *unc13A* and *unc13B* deletion mutants, respectively, normalized to controls (*unc13B* deletion: *pacdel100B; unc13*^{P84200}; *unc13A* deletion: *ems7.5/unc13*^{P84200}). The intensity levels of scaffold proteins were not altered in the mutants.

(D and E) Confocal images of calyces stained against BRP^{Nc82}, Unc13A, and Unc13B. All scale bars, 20 μm. Flies with a pan-neuronal *brp* KD in comparison to controls; staining against Unc13A (D). *Syd-1*^{null} mutants in comparison to controls; staining against Unc13B (E).

(F) Average staining intensities of BRP, Unc13A, and Unc13B in the KD or deletion situation normalized to controls show a significant downregulation of average intensity levels of Unc13A ($p = 0.000018$) and a significant upregulation of Unc13B ($p = 0.0049$) in the *brp* KD animals. Deletion of *syd-1* results in downregulation of Unc13B ($p = 0.000002$). Association tests were conducted using linear mixed models with imaging batch and animal as nested random effects. Bonferroni-corrected significance thresholds $\alpha = 0.0167$ for the *brp* KD and the *syd-1* deletion and $\alpha = 0.025$ for the *unc13A/B* deletions. Graphs as explained for Figure 1. See also Figure S3.

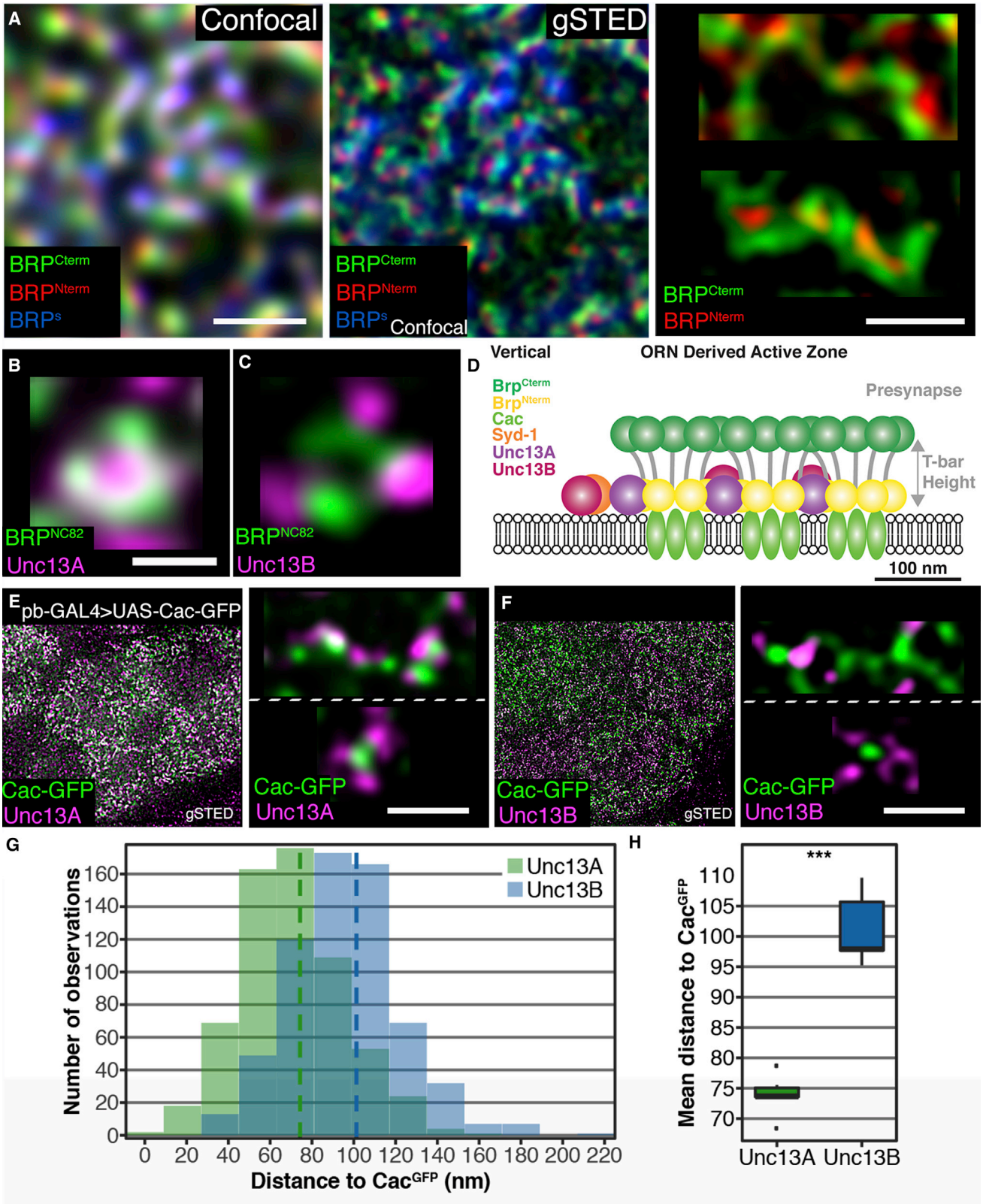

(legend on next page)

Loss of this component interferes with the fast phasic, quickly depressing release component, shifting the short-term plasticity of the SV release toward a facilitating mode (Figure 5F).

Unc13B Dominates Transmission at Slow Interneuron Synapses

LNs also contribute a major fraction of AZs in the AL. We showed (Figure 1D) that these synapses, in contrast to the ORN-to-PN synapses, display a low BRP/Syd-1 ratio and a low Unc13A level and that they express Unc13B at levels comparable to ORN-derived synapses. While ORN-to-PN synapses are fast and depressing, LN-LN synapses are rather slow and facilitating (Nagel and Wilson, 2016). To examine the role of Unc13 isoforms at LN-LN synapses, we recorded LN-derived synaptic currents after knocking down the Unc13A or B isoforms in these neurons (Figures 6A–6F). We co-expressed Channelrhodopsin (ChR2)-GFP and *unc13* isoform-specific RNAi in a subset of LNs using the NP3056-GAL4 line (Chou et al., 2010) (Figure 6A). Previous work established that light-stimulation of Channelrhodopsin results in the activation of inhibitory synaptic currents in non-ChR2-expressing LNs (Nagel and Wilson, 2016). These currents are absent in genetic controls lacking the LN driver (Nagel and Wilson, 2016); similar currents activated chemogenetically can be blocked by GABA antagonists (Liu and Wilson, 2013). To ensure that the firing pattern induced by ChR2 activation in presynaptic cells is not affected by the *unc13* knockdown itself or by accompanying developmental changes, we first recorded from GFP-positive ChR2-expressing cells. The firing pattern was the same in control and in *unc13a*/*unc13b* RNAi expressing lines (Figures 6C).

We then patched neighboring unlabeled LNs and recorded light-evoked inhibitory currents (Figure 6B). LNs were identified by their size, location, and characteristic electrophysiological properties. For example, LNs have larger cell bodies than PNs, have lower input resistances, and fire large spikes that surpass 0 mV. In contrast to ORN-to-PN synapses, where the KD of *unc13A* had the strongest effect and changed the timing of release, the KD of *unc13A* did not change the timing of release and reduced release in only a nonsignificant manner (Figures 6D–6F). The KD of *unc13B*, instead, reduced peak amplitudes and steady-state currents significantly compared to controls (Figures 6D and 6E). Notably, the time to peak remained unchanged in LNs (Figure 6F). This may reflect the method of stimulation: Single LNs form only weak synaptic connections onto neighboring LNs (Liu and Wilson, 2013) and here we used optogenetics to stimulate a large population of LNs. Alternatively, it might reflect other differences between ORN-to-PN and LN-LN synapses. The LN receptor sites, for example, could be distant to the presynaptic release sites, leading to uniformly slow responses to both Unc13A- and Unc13B-mediated release. In either case, our data indicate that Unc13B is of greater importance than Unc13A at this synapse type, consistent with their expression pattern. In contrast to the observations in ORNs, where *unc13A* KD produced the strongest effect on amplitude and slowed down release, the *unc13B* KD had a larger effect on response amplitude in the LNs.

A Generic Design Rule for Scaffold Protein/Unc13 Isoform Modules

Our electrophysiological and STED data imply collectively that domain spacing on a nanometer scale might be a major contributor to synapse diversity, at least in the *Drosophila* brain. We finally tested this hypothesis by comparing the sub-AZ spacing of Unc13A and B across synapse types directly and quantitatively. To this end, we analyzed PN-derived AZs within the calyx. Given that Unc13B is the dominant species here, we wondered whether Unc13B also resides distant from the AZ center at PN-KC synapses. The calyx microcircuitry could easily be resolved with STED analysis. The PN-derived AZs within the calycal microglomeruli form single T bars similar to the ones at NMJ synapse AZs (Christiansen et al., 2011; Yasuyama et al., 2002). Accordingly, typical donut-type BRP signals were observed using STED and Syd-1 clustered to the edge of these (Figure 7A), similarly to the ORN-derived AZs in the AL (Figure 7B). We quantified the nanodomain spacing of Unc13A and Unc13B relative to the AZ center where the Ca^{2+} channels are located (i.e., the center of the BRP rings; Figures 7C–7K). Very similar distances were found for PN- (Figures 7C–7E), ORN- (Figures 7F–7H), and non-ORN AL-derived AZs (Figures 7I–7K): Unc13B localized at a 102–115 nm distance from the center and Unc13A more centrally, at a 74–83 nm distance. These values are similar to the distances found for NMJ AZs (Böhme et al., 2016).

Taken together, the BRP/Unc13A and Syd-1/Unc13B modules appear to be stereotyped nanospacing modules for either tighter or looser coupling. Their proportions per AZ differ systematically between synapse types in the *Drosophila* brain. Thus, our analysis identified a basic principle: the AZ scaffold protein composition steers functional diversity by controlling the effective coupling distance, probably to adapt synapse types to their computational tasks within circuits. Notably, we found other essential release factors, Unc18 and Syntaxin, to be equally

Figure 4. Nanoscopic Organization of AZs at ORN-to-PN Synapses

(A) Sections of adult ALs at confocal and STED resolution. All scale bars, 500 nm. *ORCO-GAL4* > *UAS-brp-short-GFP* brains with staining against GFP (confocal resolution), $BRP^{C\text{-}Term}$ (BRP^{Nc82}), and $BRP^{N\text{-}Term}$.

(B and C) Magnified planar AZs. Scale bars, 200 nm. Staining against BRP^{Nc82} and Unc13A (B). Staining against BRP^{Nc82} and Unc13B (C).

(D) Cartoon depicting the assumed AZ composition in a side view.

(E) VA2 glomeruli in *pb-GAL4* > *UAS-Cac-GFP* flies showing GFP with an Unc13A staining. Blow-up top: magnified elongated multimeric AZ, Cac-GFP, and Unc13A. Bottom: magnified planar AZ, Cac-GFP, and Unc13A.

(F) VA2 glomeruli in *pb-GAL4* > *UAS-Cac-GFP* flies showing GFP with an Unc13B staining. Blow-up top: magnified elongated multimeric AZ, Cac-GFP, and Unc13B. Bottom: magnified planar AZ, Cac-GFP, and Unc13B.

(G) Histogram of distance bins of either Unc13A to Cac-GFP (green) or Unc13B to Cac-GFP (blue).

(H) Unc13B is further away from Cac-GFP than Unc13A is, $p = 9.99 \times 10^{-15}$, n = 619 measurements for Unc13A and n = 647 for Unc13B across six animals each. Association tests were conducted using linear mixed models with scan, hemisphere, and animal as nested random effects. Graphs as explained for Figure 1.

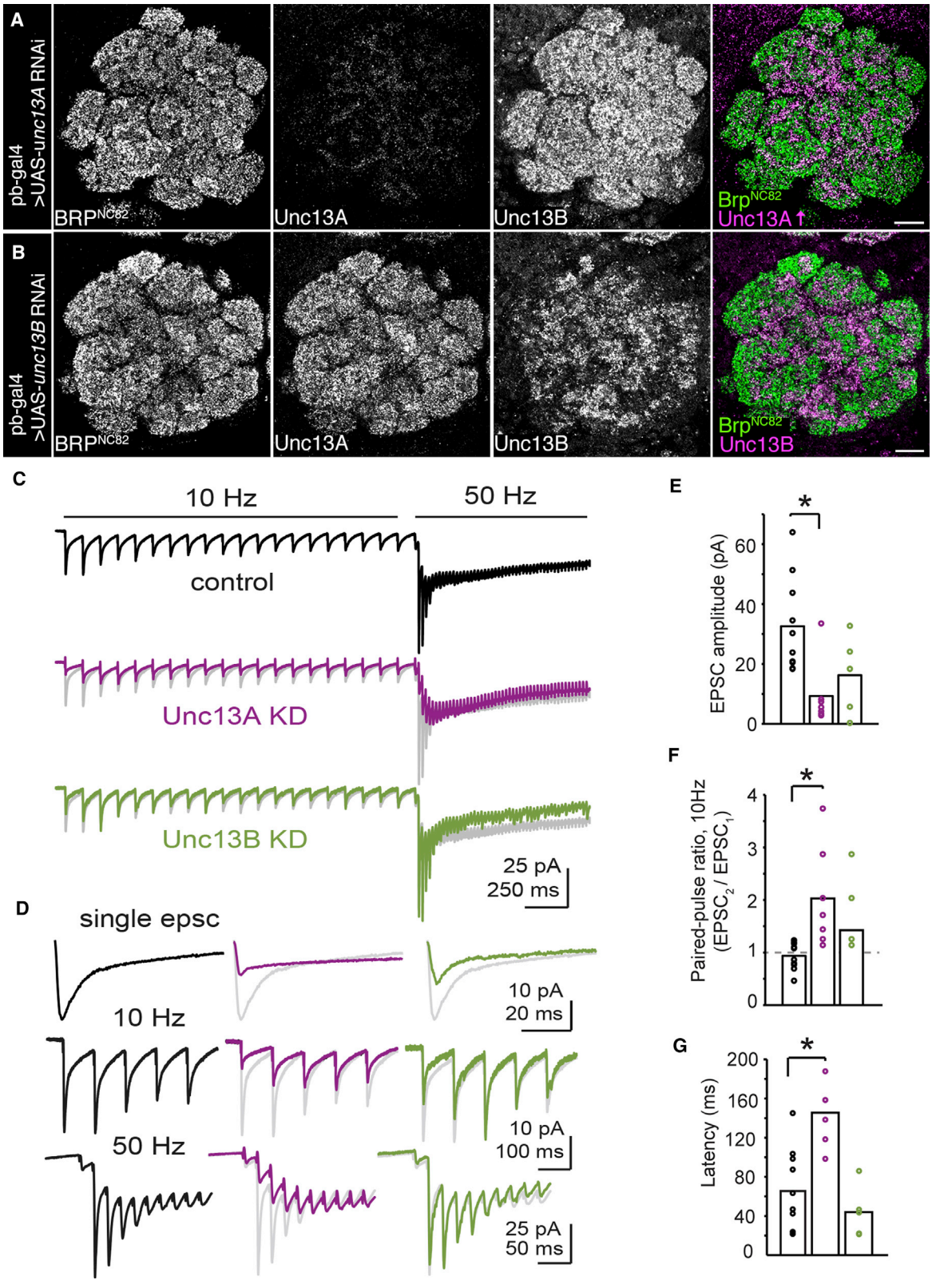

(legend on next page)

distributed over the AZ population of the *Drosophila* brain (Figure S6), emphasizing the specific role of Unc13 family proteins in AZ diversity, at least in this system.

DISCUSSION

Synapses are highly specialized structures mediating the flow of information between neurons and are thought to be cellular substrates for learning and memory. One hallmark of synapses is their functional heterogeneity: synapses can exhibit either high or low transmission fidelity and this diversity results in synapse-specific differences in response kinetics and short-term plasticity. Functional synaptic diversity, particularly regarding synaptic short-term plasticity, is considered critical for routing and encoding sensory information within neuron networks in the brain (Chabrol et al., 2015; Jackman and Regehr, 2017). It plays a major role in the temporal coding of multisensory integration and extraction of specific sensory features. Accordingly, specific synaptic alterations can result in devastating neurological and psychiatric diseases.

Functional synaptic diversity is influenced by pre- and postsynaptic factors: the number, density and location of SVs, VGCCs, receptors, and fusion machinery proteins (O'Rourke et al., 2012). Specific interactions between these molecular players at the nanometer ("nanoscale") level are believed to define synaptic efficacy and plasticity. Presynaptic factors, particularly the physical distance between presynaptic VGCCs and the sensor for SV fusion, determine the functional coupling distance that influences release probability and, hence, short-term plasticity (Eggermann et al., 2011). Indeed, this coupling varies widely across synapses. Tight coupling has been associated with high release probability and synaptic depression, but loose coupling with low release probabilities and greater paired-pulse facilitation (Eggermann et al., 2011; Vyleta and Jonas, 2014). However, despite the physiological evidence of this kind of presynaptic diversity for brain function, its cellular and molecular underpinnings are poorly understood. Consequently, deciphering the molecular basis of synaptic functional diversity has been named as a major challenge remaining in synapse research (Südhof, 2012). Here, we find evidence for a generic molecular principle that regulates coupling strength to generate functional diversity at *Drosophila* central synapses.

Nanoscopic Scaffold Diversity Tunes Release Probability and Short-Term Plasticity

Short-term plasticity causes synapses to act as temporal filters, allowing them to transmit a certain range of signal frequencies preferentially. Excitatory and inhibitory neurons especially often show distinct forms of short-term plasticity, as do synapses from the same cell onto different types of interneurons (Beierlein et al., 2003; Stokes and Isaacson, 2010). However, the molecular basis of this synaptic diversity remained mysterious, making it difficult to interrogate the function of this diversity in a circuit context. Here, we show that in the *Drosophila* olfactory system, expression of *unc13* isoforms and their corresponding scaffolding proteins correlates with temporal properties of synaptic transmission.

The first relay synapse of the *Drosophila* olfactory system displays a particularly high release probability (Kazama and Wilson, 2008). We found that this synapse is enriched for BRP/Unc13A complexes, and expression of *unc13A* is required for its high release probability. This was evident from the complete abrogation of fast, phasic post-synaptic currents when this specific Unc13 isoform was specifically reduced. Although this first synapse in the *Drosophila* olfactory system exhibits short-term depression due to its high release probability, it still transmits broadband signals, consistent with our finding that *unc13B* is expressed uniformly across the AL and that a slow component of transmission remains after *unc13A* KD. Interestingly, previous work using different pharmacological blockers of nicotinic acetylcholine (ACh) receptors could separate two components of evoked post-synaptic current—one with a fast, the other with a much lower rate of depression (Nagel et al., 2015). Thus, the fast, depressing, Unc13A-mediated release component might be matched by a different ACh receptor than the slow Unc13B component.

In contrast to ORN-to-PN synapses, AL synapses originating from LNs are slow and facilitating (Liu and Wilson, 2013; Nagel et al., 2015; Nagel and Wilson, 2016). Accordingly, we observed

Figure 5. Unc13A and Unc13B Isoforms Play Distinct Roles in Synaptic Transmission at ORN-to-PN Synapses

(A and B) Confocal sections of adult ALs. All scale bars, 10 μm. Staining against BRP^{Nc82}, Unc13A, and Unc13B in *pb-GAL4* > *UAS-unc13A* RNAi flies. The Unc13A brightness was increased in the merged image for visibility (A). Anti-BRP^{Nc82}, Unc13A, and Unc13B staining in *pb-GAL4* > *UAS-unc13B* RNAi flies (B).

(C) Group-averaged evoked synaptic currents in control (n = 10 cells), *unc13A* KD (n = 7 cells), and *unc13B* KD (n = 5 cells) flies during 10 Hz and 50 Hz stimulation of the antennal nerve. The average response from control recordings is shown in gray behind the average *unc13A* KD and *unc13B* KD traces for direct comparison.

(D) Group-averaged data from (C) showing the first EPSC (top), the onset of the 10 Hz response (middle), and the onset of 50 Hz response (bottom), reproduced on zoomed-in timescales. In (C) and (D), stimulus artifacts were minimized for clarity by linearly extrapolating between the pre- and post-stimulation artifact periods, typically 2–3 ms. At the transition from 10 Hz to 50 Hz stimulation, there is facilitation of the EPSC amplitude in control and *unc13B* KD experiments. This property is lost following *unc13A* KD and varies across cells.

(E) Quantification of the first EPSC amplitude across genotypes. EPSC amplitudes were significantly different between groups ($F = 6.28$; $p < 0.01$, one-way ANOVA with Tukey post hoc comparison). The first EPSC was significantly smaller in *unc13A* KD flies than in controls ($p < 0.01$, unpaired Student's t test) and not significantly reduced after *unc13B* KD.

(F) Quantification of the paired-pulse ratio during 10 Hz stimulation across genotypes. The paired-pulse ratio varied between groups ($F = 6.21$; $p < 0.01$, one-way ANOVA with Tukey post hoc comparison). The paired-pulse ratio was significantly elevated in *unc13A* KD flies ($p < 0.01$, unpaired Student's t test), but not in *unc13B* KD.

(G) The latency to peak evoked current from the onset of 50 Hz stimulation. The time to peak current was different between groups ($F = 15.07$; $p < 0.001$, one-way ANOVA with Tukey post hoc comparison), and was increased relative to controls in *unc13A* KD flies ($p < 0.001$). Bar charts represent mean values.

See also Figures S4 and S5.

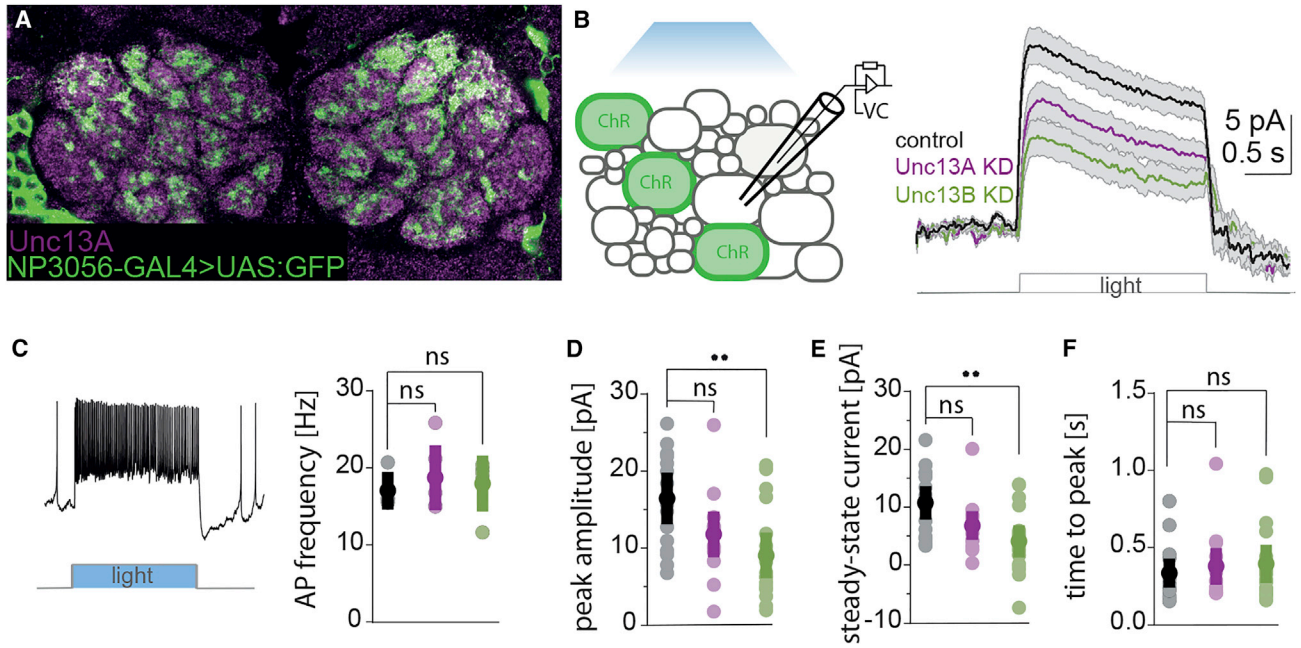

Figure 6. An *Unc13B* Knockdown in Unc13B-Dominated LN:LN Synapses Drastically Reduces Release Amplitude

(A) Staining against Unc13A and anti-GFP in the fly AL. The GFP-positive LNs barely show an Unc13A signal.

(B) Scheme of the experimental procedure. Left: recordings were made from LNs postsynaptic to Channelrhodopsin 2 ($ChR2^+$, GFP^+) expressing cells. Voltage command (VC, right) measured average postsynaptic currents in response to optogenetical activation of the presynapse ($ChR2^+$) in control (n = 15), *unc13A* KD (n = 13), and *unc13B* KD (n = 18) flies. Traces are mean ± SEM.

(C) Whole-cell current-clamp recordings of presynaptic ($ChR2^+$, GFP^+) LNs. Left: example of a spike train in presynaptic LNs evoked by a light pulse. Right: light-evoked firing rate of Channelrhodopsin-expressing cells over a 2-s stimulation period. The action potential frequency in presynaptic LNs ($ChR2^+$) is not affected by the expression of *unc13A*/*unc13B*-RNAi constructs. (Kruskal-Wallis test, ns = not significant). From left to right: controls (black), *unc13A* KD (magenta), *unc13B* (green).

(D) Average peak amplitudes of postsynaptic currents are significantly different between control and *unc13B* KD flies (Kruskal-Wallis followed by Dunn's multiple comparison test, Bonferroni-corrected, controls (black): n = 16, *unc13A* KD (magenta): n = 14, outliers were removed with the fourth spread method [Devore, 2011], p = 0.069, *unc13B* KD (green): n = 18, p = 0.001).

(E) Average steady-state current (SSC) measured at 1.5 s after light onset, averaged over a period of 0.5 s. SSC was significantly smaller in *unc13B* KD flies compared to control animals (Kruskal-Wallis followed by Dunn's multiple comparison test, Bonferroni-corrected, controls (black): n = 16, *unc13A* KD (magenta): n = 15, p = 0.10, *unc13B* KD (green): n = 18, p = 0.001).

(F) Time until outward currents reached the maximum after onset of the light stimulus. The time to reach the peak amplitude remained the same in all of the recorded groups (Kruskal-Wallis followed by Dunn's multiple comparison test, Bonferroni-corrected, controls (black): n = 16, *unc13A* KD (magenta): n = 14, outliers were removed with the fourth spread method, p = 0.83, *unc13B* KD (green): n = 18, p = 0.79). Values represent mean ± SD.

that these synapses are low in Unc13A and that, although *unc13A* KD tended to affect LN-LN synaptic signals as well, *unc13B* KD had a stronger effect on LN-LN synaptic transmission, indicating a more prominent role for Unc13B at these synapses. Interestingly, the slow time course of transmission was unchanged in either KD situation. This could be an artifact caused by the optogenetic stimulation protocol. However, this is unlikely, as the latency to the first light-induced spike was short in all presynaptic LN recordings (Figure 6C). Another possibility is that postsynaptic factors also contribute to the slowness of these synapses.

The second relay synapse of the olfactory system (PN-KC synapses) transmits high-frequency signals typical for PNs (>100 Hz), is slow and integrates convergent signals (Gruntman and Turner, 2013). Our finding that Unc13B (and accordingly also Syd-1) is particularly prominent at this synapse implies strongly that these synapses are, by their nanoscopic design, tuned toward a facilitating low depression mode, which might well be instrumental to their computational role. Future studies integrating behavioral and electrophysiological analyses at this synapse are warranted to explore this hypothesis.

Toward a "Nanoscopic Code" of Synapse Diversity for Circuit Modeling

An obvious question is how this cellular and molecular diversity is instructed; whether it takes place as a cell-autonomous function of the respective presynaptic neuron or whether postsynaptic partner neurons are involved in the developmental setup of molecular AZ diversity. Postsynaptic targeting specificity has been observed electrophysiologically in mouse neocortex at the AZs of pyramidal cells, connected to two classes of postsynaptic GABAergic neurons (Beierlein et al., 2003; Reyes et al., 1998). The *Drosophila* system with its unique possibilities for genetic intervention should be an ideal model for studying cellular

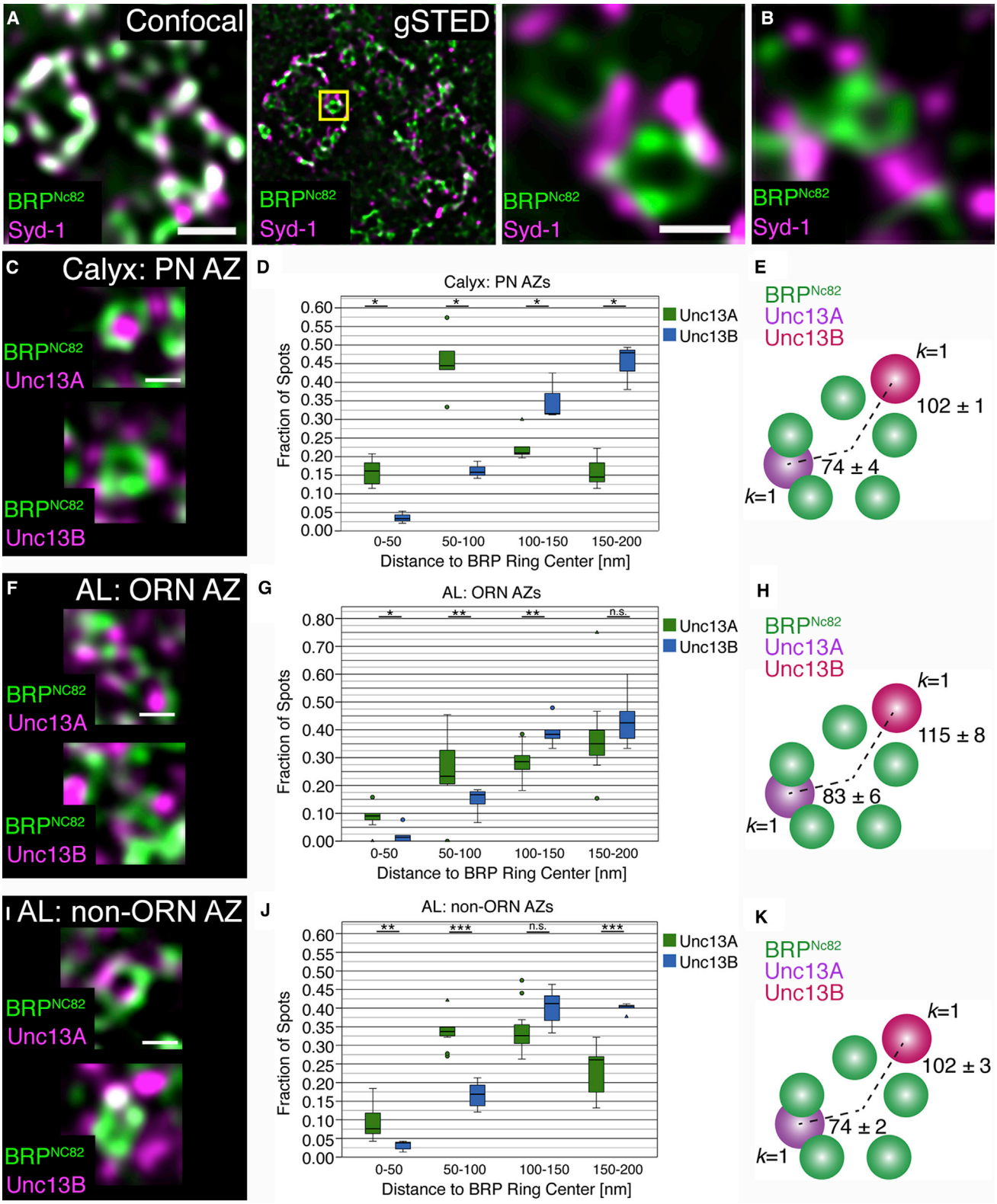

Figure 7. Comparative STED Analysis for ORN-, LN-, and PN-Derived AZs

(A) Magnified section of an adult wild-type calyx imaged by conventional confocal (left) and time-gated STED (gSTED) microscopy. Scale bar, 500 nm.

(B) Staining against BRP^{Nc82} and Syd-1. The magnified insets show a planar AZ within the calyx microglomeruli and in the AL. Scale bar, 200 nm.

(legend continued on next page)

interactions systematically in the context of establishing synaptic diversity. Cell adhesion proteins, for example, the newly discovered teneurins (Hong et al., 2012; Mosca and Luo, 2014) or LRP4 (Mosca et al., 2017), are attractive candidates for instructing and maintaining AZ diversity via scaffold protein clustering. Interestingly, postsynaptically expressed cell adhesion proteins have been shown to instruct short-term plasticity at hippocampal synapses (Sylwestrak and Ghosh, 2012). It will be interesting to see whether these regulations might involve differential spacing of (M)Unc13 isoforms.

Electron microscopy has been used recently to systematically reconstruct both the AL (Berck et al., 2016) and downstream integrative centers mediating olfactory learning and memory processes (Takemura et al., 2017). In these studies, the electron-dense AZ scaffold ("T bar") was used as the crucial landmark to identify AZs and, consequently, synaptic connections between reconstructed neurons. Although this complete wiring diagram will clearly help bridging the gap between circuits and behavior, a satisfactory understanding and functional modeling of circuits will also depend on an in-depth knowledge of specific features of the synapse types present. We are confident that the "nanoscopic molecular fingerprints" of synapses, which we started to provide here using the abundances and ratios of specific presynaptic proteins, will be helpful in assessing specific synaptic features.

Scaffold Protein Composition Tuning Functional Diversity: a Generic Design Principle?

Will our results generalize to the mammalian brain? Our recent analysis demonstrated that Unc13 nanoclusters function topologically to generate stable SV release sites, with their defined spacing ensuring determined and reliable timing of SV release (Reddy-Alla et al., 2017). Moreover, a dramatic decrease of synaptic transmission upon disruption of the AZ scaffold has been described in several model systems (BRP/RBP in *Drosophila* and RIM/RBP or RIM/ELKS in mouse); this observed decrease is in line with a loss of release sites, which was paralleled by a severe reduction of Munc13/Unc13A in all cases (Acuna et al., 2016; Böhme et al., 2016; Wang et al., 2016).

Despite these analogies, future analyses will have to clarify to which degree the exact details of the molecular interactions between scaffold proteins and (M)Unc13 release factors have been conserved. For example, we do currently not know whether the mammalian Syd-1 homologs (Wentzel et al., 2013) are involved in clustering Munc13 isoforms as well. Moreover, given the different structural organization of the Unc13 family N termini, the details of the molecular interactions used in AZ localization and scaffold binding have likely changed over evolutionary time. While a generic role of AZ scaffolds in localizing and stabilizing release sites generated by Unc13 appears probable, modifications in the molecular setup might have led to evolutionary diversified discrete "solutions". Notably, our findings illustrate how functional diversity might be executed varying the amounts of the same proteins (Nusser, 2018).

Previous work at *C. elegans* and *Drosophila* neuromuscular synapses have described a "linear assembly pathway" with Syd-1 targeting BRP/ELKS complexes into growing AZs (Dai et al., 2006; Owald et al., 2010). The fact that BRP/Syd-1 ratios are diversified between *Drosophila* CNS synapses now requires for modifications of this scheme. While a specific Neurexin-Neuroligin pair operating in conjunction with Syd-1 is crucial for NMJ synapse assembly, the evolutionary diversification of similar cell adhesion molecules might contribute to diversifying AZ assembly schemes.

Considerable biophysical evidence supports the diversification of coupling distances at mammalian synapses (Eggermann et al., 2011). Notably, seminal experiments, where Munc13 isoforms were expressed in cultured hippocampal neurons in a *munc13* null mutant background, have already shown that mammalian Munc13 isoforms differentially control release probability and short-term plasticity and, thus, contribute to the heterogeneity of synaptic information coding (Rosenmund et al., 2002). It should, therefore, be explored whether differential VGCC-coupling of these mammalian Munc13 isoforms also contributes to the functional diversity of synapses in the rodent brain. The well-documented interactions between the canonical AZ scaffold proteins and the extended, evolutionarily diversified N termini of Munc13 family proteins (Deng et al., 2011; Hu et al., 2013; Kawabe et al., 2017; Zhou et al., 2013) have a good chance to be critical for the definition of release sites in a generic manner, and could provide diversification by their differential coupling to Ca^{2+} channels. Notably, the mammalian BRP homolog ELKS was shown to be involved in the clustering of specific Munc13 isoforms (Kawabe et al., 2017).

Our results collectively elucidate a comparatively simple "molecular syntax" that explains synapse functional diversity in a

(C) Planar view of BRP^{Nc82} and Unc13A (above) or Unc13B (below) at a PN AZ in the calyx (gSTED). Scale bar, 200 nm.
(D and E) Cluster distance (D) and *k* nearest-neighbor analysis (E). Boxplot shows the number of Unc13A and Unc13B puncta at defined distances to the center of the BRP ring, normalized to the total number of puncta for each isoform up to 200 nm from the BRP ring center (D; Unc13A: n = 5 brains, 190 AZs; Unc13B: n = 3 brains, 150 AZs). (E) Scheme representing the *k* nearest-neighbor analysis ($k = 1$). At the PN AZs, the first Unc13A spot was found closer to the BRP ring center than any Unc13B spot ($p < 0.05$, Mann-Whitney U (MWU) test).
(F) Planar view of BRP^{Nc82} and Unc13A (upper) or Unc13B (lower) at ORN-derived AZs (gSTED). Note the concatameric structure of the BRP rings. Scale bar, 200 nm.
(G) Cluster distance analysis at ORN AZs in the AL as in (D; Unc13A: n = 11 brains, 128 AZs; Unc13B: n = 5 brains, 97 AZs).
(H) Scheme representing the *k* nearest-neighbor analysis ($k = 1$). At the ORN AZs, the first Unc13A spot was found closer to the BRP ring center than any Unc13B spot ($p < 0.01$, MWU test).
(I) Example of gSTED images of BRP^{Nc82} and Unc13A (upper) or Unc13B (lower) in planar view at non-ORN AZs in the AL. Scale bar, 200 nm.
(J) Cluster distance analysis at non ORN AZs in the AL as in (D; Unc13A: n = 11 brains, 446 AZs; Unc13B: n = 5 brains, 298 AZs).
(K) Scheme representing the *k* nearest-neighbor analysis ($k = 1$). At the non-ORN synapses in the AL, the first Unc13A spot was found closer to the BRP ring center than any Unc13B spot ($p < 0.001$, MWU test). *$p < 0.05$, **$p < 0.01$, ***$p < 0.001$, ns, not significant, Mann-Whitney U (MWU) tests. Values indicate mean ± SEM. Graphs as explained for Figure 1.

systematic manner. Our nanoscopic fingerprints contain unique information crucial to integrate the electrophysiological, ultrastructural, and molecular analyses of synapses, and could, thus, become of real importance for our analysis of both the healthy and the diseased brain.

EXPERIMENTAL PROCEDURES

Further details and an outline of resources used in this work can be found in Supplemental Experimental Procedures.

Animal Rearing and Fly Strains

Fly strains were reared under standard laboratory conditions (Sigrist et al., 2003) at 25°C, 65%–70% humidity and constant 12/12 hr light/dark cycle in incubators. If not stated differently, 4–7 days female flies were used for the experiments.

Immunohistochemistry, Image Acquisition, and Analysis

Immunohistochemistry was performed according to our standard protocol (Andlauer et al., 2014). Conventional confocal and STED images were acquired with a TCS SP8 and TCS SP8 gSTED 3× microscope (Leica Microsystems, Wetzlar, Germany), respectively.

Electrophysiology

Whole-cell patch-clamp recordings from PNs and LNs were made as described in Nagel et al. (2015) and Nagel and Wilson (2016). LNs were identified based on morphology and electrophysiological properties.

Statistics

Antibody ratios were calculated using custom ImageJ plugins (http://ratios.andlauer.net). Normalized median ratios were compared using Mann-Whitney U tests in R v3.3.3.

Intensity (e.g., knockdowns and deletions) data as well as STED punctae distances were analyzed in R with linear mixed models using nested random effects; the associations were confirmed using non-parametric permutation tests.

For cluster distance analyses, statistical tests were conducted in SPSS (IBM, Armonk, USA). The nonparametric Mann-Whitney U test was used for analyses.

For colocalization analyses, Spearman rank correlation coefficients were compared using the paired Wilcoxon signed-rank test. For electrophysiological analyses, comparisons between groups were performed by Kruskal Wallis or one-way ANOVA tests, as indicated in the text.

SUPPLEMENTAL INFORMATION

Supplemental Information includes Supplemental Experimental Procedures and six figures and can be found with this article online at https://doi.org/10.1016/j.celrep.2018.03.126.

ACKNOWLEDGMENTS

We thank Madeleine Brünner, Christine Quentin, and Anastasia Stawrakakis for excellent technical assistance. We also thank the Cellular Imaging Facility of the Leibniz Institute for Molecular Pharmacology and the Core Facility BioSupraMol of the Freie Universität Berlin for training, discussion, and support on the Leica TCS gSTED and the TCS SP8 systems. This work was supported by grants from the Deutsche Forschungsgemeinschaft (DFG) (Exc 257, TP A3 and A06 SFB958, and TP09 SFB740) to S.J.S. and to A.M.W (Emmy Noether Program), and from NIH (R01MH109690), NSF (IOS1555933), and the NYU Whitehead Fellowship program to K.N. T.F.M.A. was supported by the German Federal Ministry of Education and Research (BMBF) through the Integrated Network IntegraMent, under the auspices of the e:Med Programme (01ZX1614J).

AUTHOR CONTRIBUTIONS

A.F., T.F.M.A, K.N., and S.J.S. designed the study. A.F., T.F.M.A, A.E., M.M., K.E., and J.W. performed the experiments. A.F., T.F.M.A, A.E., M.M., K.E., J.W., and A.M.W. analyzed the data. T.F.M.A., M.L., T.M.-R., J.R.P.G., and A.M.W. provided protocols, reagents, and advice. All the authors commented on the manuscript. A.F., T.F.M.A, M.M., A.E., K.N., and S.J.S wrote the manuscript.

DECLARATION OF INTERESTS

The authors declare no competing interests.

Received: November 28, 2017
Revised: February 28, 2018
Accepted: March 27, 2018
Published: May 1, 2018

REFERENCES

Acuna, C., Liu, X., and Südhof, T.C. (2016). How to make an active zone: unexpected universal functional redundancy between RIMs and RIM-BPs. Neuron *91*, 792–807.

Andlauer, T.F., Scholz-Kornehl, S., Tian, R., Kirchner, M., Babikir, H.A., Depner, H., Loll, B., Quentin, C., Gupta, V.K., Holt, M.G., et al. (2014). Drep-2 is a novel synaptic protein important for learning and memory. eLife *3*, e03895.

Beierlein, M., Gibson, J.R., and Connors, B.W. (2003). Two dynamically distinct inhibitory networks in layer 4 of the neocortex. J. Neurophysiol. *90*, 2987–3000.

Berck, M.E., Khandelwal, A., Claus, L., Hernandez-Nunez, L., Si, G., Tabone, C.J., Li, F., Truman, J.W., Fetter, R.D., Louis, M., et al. (2016). The wiring diagram of a glomerular olfactory system. eLife *5*, e14859.

Böhme, M.A., Beis, C., Reddy-Alla, S., Reynolds, E., Mampell, M.M., Grasskamp, A.T., Lützkendorf, J., Bergeron, D.D., Driller, J.H., Babikir, H., et al. (2016). Active zone scaffolds differentially accumulate Unc13 isoforms to tune Ca(2+) channel-vesicle coupling. Nat. Neurosci. *19*, 1311–1320.

Chabrol, F.P., Arenz, A., Wiechert, M.T., Margrie, T.W., and DiGregorio, D.A. (2015). Synaptic diversity enables temporal coding of coincident multisensory inputs in single neurons. Nat. Neurosci. *18*, 718–727.

Chou, Y.H., Spletter, M.L., Yaksi, E., Leong, J.C., Wilson, R.I., and Luo, L. (2010). Diversity and wiring variability of olfactory local interneurons in the Drosophila antennal lobe. Nat. Neurosci. *13*, 439–449.

Christiansen, F., Zube, C., Andlauer, T.F., Wichmann, C., Fouquet, W., Owald, D., Mertel, S., Leiss, F., Tavosanis, G., Luna, A.J., et al. (2011). Presynapses in Kenyon cell dendrites in the mushroom body calyx of Drosophila. J. Neurosci. *31*, 9696–9707.

Dai, Y., Taru, H., Deken, S.L., Grill, B., Ackley, B., Nonet, M.L., and Jin, Y. (2006). SYD-2 Liprin-alpha organizes presynaptic active zone formation through ELKS. Nat. Neurosci. *9*, 1479–1487.

Deng, L., Kaeser, P.S., Xu, W., and Südhof, T.C. (2011). RIM proteins activate vesicle priming by reversing autoinhibitory homodimerization of Munc13. Neuron *69*, 317–331.

Devore, J.L. (2011). Probability and Statistics for Engineering and the Sciences (Cengage Learning).

Eggermann, E., Bucurenciu, I., Goswami, S.P., and Jonas, P. (2011). Nanodomain coupling between Ca^{2+} channels and sensors of exocytosis at fast mammalian synapses. Nat. Rev. Neurosci. *13*, 7–21.

Fouquet, W., Owald, D., Wichmann, C., Mertel, S., Depner, H., Dyba, M., Hallermann, S., Kittel, R.J., Eimer, S., and Sigrist, S.J. (2009). Maturation of active zone assembly by Drosophila Bruchpilot. J. Cell Biol. *186*, 129–145.

Gjorgjieva, J., Drion, G., and Marder, E. (2016). Computational implications of biophysical diversity and multiple timescales in neurons and synapses for circuit performance. Curr. Opin. Neurobiol. *37*, 44–52.

Gruntman, E., and Turner, G.C. (2013). Integration of the olfactory code across dendritic claws of single mushroom body neurons. Nat. Neurosci. *16*, 1821–1829.

Hong, W., Mosca, T.J., and Luo, L. (2012). Teneurins instruct synaptic partner matching in an olfactory map. Nature *484*, 201–207.

Hu, Z., Tong, X.J., and Kaplan, J.M. (2013). UNC-13L, UNC-13S, and Tomosyn form a protein code for fast and slow neurotransmitter release in Caenorhabditis elegans. eLife *2*, e00967.

Jackman, S.L., and Regehr, W.G. (2017). The mechanisms and functions of synaptic facilitation. Neuron *94*, 447–464.

Kawabe, H., Mitkovski, M., Kaeser, P.S., Hirrlinger, J., Opazo, F., Nestvogel, D., Kalla, S., Fejtova, A., Verrier, S.E., Bungers, S.R., et al. (2017). ELKS1 localizes the synaptic vesicle priming protein bMunc13-2 to a specific subset of active zones. J. Cell Biol. *216*, 1143–1161.

Kazama, H., and Wilson, R.I. (2008). Homeostatic matching and nonlinear amplification at identified central synapses. Neuron *58*, 401–413.

Kazama, H., and Wilson, R.I. (2009). Origins of correlated activity in an olfactory circuit. Nat. Neurosci. *12*, 1136–1144.

Kittel, R.J., Wichmann, C., Rasse, T.M., Fouquet, W., Schmidt, M., Schmid, A., Wagh, D.A., Pawlu, C., Kellner, R.R., Willig, K.I., et al. (2006). Bruchpilot promotes active zone assembly, Ca2+ channel clustering, and vesicle release. Science *312*, 1051–1054.

Kremer, M.C., Christiansen, F., Leiss, F., Paehler, M., Knapek, S., Andlauer, T.F., Förstner, F., Kloppenburg, P., Sigrist, S.J., and Tavosanis, G. (2010). Structural long-term changes at mushroom body input synapses. Curr. Biol. *20*, 1938–1944.

Liu, W.W., and Wilson, R.I. (2013). Glutamate is an inhibitory neurotransmitter in the Drosophila olfactory system. Proc. Natl. Acad. Sci. USA *110*, 10294–10299.

Mosca, T.J., and Luo, L. (2014). Synaptic organization of the Drosophila antennal lobe and its regulation by the Teneurins. eLife *3*, e03726.

Mosca, T.J., Luginbuhl, D.J., Wang, I.E., and Luo, L. (2017). Presynaptic LRP4 promotes synapse number and function of excitatory CNS neurons. eLife *6*, e27347.

Nagel, K.I., and Wilson, R.I. (2016). Mechanisms underlying population response dynamics in inhibitory interneurons of the Drosophila antennal lobe. J. Neurosci. *36*, 4325–4338.

Nagel, K.I., Hong, E.J., and Wilson, R.I. (2015). Synaptic and circuit mechanisms promoting broadband transmission of olfactory stimulus dynamics. Nat. Neurosci. *18*, 56–65.

Nusser, Z. (2018). Creating diverse synapses from the same molecules. Curr. Opin. Neurobiol. *51*, 8–15.

O'Rourke, N.A., Weiler, N.C., Micheva, K.D., and Smith, S.J. (2012). Deep molecular diversity of mammalian synapses: why it matters and how to measure it. Nat. Rev. Neurosci. *13*, 365–379.

Owald, D., Fouquet, W., Schmidt, M., Wichmann, C., Mertel, S., Depner, H., Christiansen, F., Zube, C., Quentin, C., Körner, J., et al. (2010). A Syd-1 homologue regulates pre- and postsynaptic maturation in Drosophila. J. Cell Biol. *188*, 565–579.

Petzoldt, A.G., Lützkendorf, J., and Sigrist, S.J. (2016). Mechanisms controlling assembly and plasticity of presynaptic active zone scaffolds. Curr. Opin. Neurobiol. *39*, 69–76.

Reddy-Alla, S., Böhme, M.A., Reynolds, E., Beis, C., Grasskamp, A.T., Mampell, M.M., Maglione, M., Jusyte, M., Rey, U., Babikir, H., et al. (2017). Stable positioning of Unc13 restricts synaptic vesicle fusion to defined release sites to promote synchronous neurotransmission. Neuron *95*, 1350–1364.

Reyes, A., Lujan, R., Rozov, A., Burnashev, N., Somogyi, P., and Sakmann, B. (1998). Target-cell-specific facilitation and depression in neocortical circuits. Nat. Neurosci. *1*, 279–285.

Rosenmund, C., Sigler, A., Augustin, I., Reim, K., Brose, N., and Rhee, J.S. (2002). Differential control of vesicle priming and short-term plasticity by Munc13 isoforms. Neuron *33*, 411–424.

Rybak, J., Talarico, G., Ruiz, S., Arnold, C., Cantera, R., and Hansson, B.S. (2016). Synaptic circuitry of identified neurons in the antennal lobe of Drosophila melanogaster. J. Comp. Neurol. *524*, 1920–1956.

Sakamoto, H., Ariyoshi, T., Kimpara, N., Sugao, K., Taiko, I., Takikawa, K., Asanuma, D., Namiki, S., and Hirose, K. (2018). Synaptic weight set by Munc13-1 supramolecular assemblies. Nat. Neurosci. *21*, 41–49.

Schmid, A., Hallermann, S., Kittel, R.J., Khorramshahi, O., Frölich, A.M., Quentin, C., Rasse, T.M., Mertel, S., Heckmann, M., and Sigrist, S.J. (2008). Activity-dependent site-specific changes of glutamate receptor composition in vivo. Nat. Neurosci. *11*, 659–666.

Sigrist, S.J., Reiff, D.F., Thiel, P.R., Steinert, J.R., and Schuster, C.M. (2003). Experience-dependent strengthening of Drosophila neuromuscular junctions. J. Neurosci. *23*, 6546–6556.

Spühler, I.A., Conley, G.M., Scheffold, F., and Sprecher, S.G. (2016). Super resolution imaging of genetically labeled synapses in Drosophila brain tissue. Front. Cell. Neurosci. *10*, 142.

Stanley, E.F. (2016). The nanophysiology of fast transmitter release. Trends Neurosci. *39*, 183–197.

Stokes, C.C., and Isaacson, J.S. (2010). From dendrite to soma: dynamic routing of inhibition by complementary interneuron microcircuits in olfactory cortex. Neuron *67*, 452–465.

Südhof, T.C. (2012). The presynaptic active zone. Neuron *75*, 11–25.

Sylwestrak, E.L., and Ghosh, A. (2012). Elfn1 regulates target-specific release probability at CA1-interneuron synapses. Science *338*, 536–540.

Takemura, S.Y., Aso, Y., Hige, T., Wong, A., Lu, Z., Xu, C.S., Rivlin, P.K., Hess, H., Zhao, T., Parag, T., et al. (2017). A connectome of a learning and memory center in the adult *Drosophila* brain. eLife *6*, e26975.

Vyleta, N.P., and Jonas, P. (2014). Loose coupling between Ca2+ channels and release sensors at a plastic hippocampal synapse. Science *343*, 665–670.

Wadel, K., Neher, E., and Sakaba, T. (2007). The coupling between synaptic vesicles and Ca2+ channels determines fast neurotransmitter release. Neuron *53*, 563–575.

Wang, S.S.H., Held, R.G., Wong, M.Y., Liu, C., Karakhanyan, A., and Kaeser, P.S. (2016). Fusion competent synaptic vesicles persist upon active zone disruption and loss of vesicle docking. Neuron *91*, 777–791.

Wentzel, C., Sommer, J.E., Nair, R., Stiefvater, A., Sibarita, J.B., and Scheiffele, P. (2013). mSYD1A, a mammalian synapse-defective-1 protein, regulates synaptogenic signaling and vesicle docking. Neuron *78*, 1012–1023.

Wilson, R.I. (2013). Early olfactory processing in Drosophila: mechanisms and principles. Annu. Rev. Neurosci. *36*, 217–241.

Yasuyama, K., Meinertzhagen, I.A., and Schürmann, F.W. (2002). Synaptic organization of the mushroom body calyx in Drosophila melanogaster. J. Comp. Neurol. *445*, 211–226.

Zhou, K., Stawicki, T.M., Goncharov, A., and Jin, Y. (2013). Position of UNC-13 in the active zone regulates synaptic vesicle release probability and release kinetics. eLife *2*, e01180.

Cell Reports, Volume *23*

Supplemental Information

Active Zone Scaffold Protein Ratios Tune Functional Diversity across Brain Synapses

Andreas Fulterer, Till F.M. Andlauer, Anatoli Ender, Marta Maglione, Katherine Eyring, Jennifer Woitkuhn, Martin Lehmann, Tanja Matkovic-Rachid, Joerg R.P. Geiger, Alexander M. Walter, Katherine I. Nagel, and Stephan J. Sigrist

Supplemental Information

Supplemental Data Items

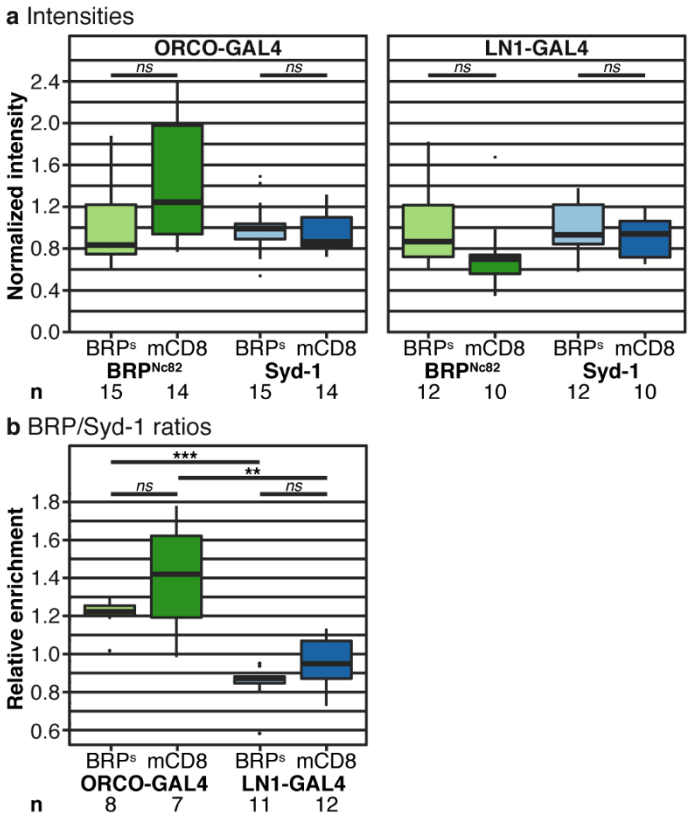

Figure S1: Expression of *brp-short* does not significantly alter the intensities or ratios of scaffold proteins, related to Figure 1

Analysis of staining intensities and antibody ratios. Either brp-short-GFP or mCD8-GFP was expressed using either ORCO-GAL4 (left) or LN1-GAL4 (right). Sample sizes (n) are indicated at the bottom of the plots.

(a) Average staining intensities of BRP and Syd-1 in ALs. For each driver line, normalized intensities of BRP and Syd-1 did not significantly differ between the two GFP fusion proteins used. Average intensities for mCD8-GFP were normalized to BRP-short-GFP intensities. Association tests were conducted using linear mixed models with imaging batch and animal as nested random effects. The Bonferroni-corrected significance threshold was $\alpha = 0.025$ for each GAL4 line. ORCO-GAL4: BRP^{Nc82} $p = 0.15$, Syd-1 $p = 0.58$; LN1-GAL4: BRP^{Nc82} $p = 0.13$, Syd-1 $p = 0.39$. BRPs = BRP-short.

(b) Analysis of median BRP/Syd-1 ratios in ALs. GFP-positive median ratios were normalized by median ratios of the surrounding AL to illustrate the relative difference between GFP-positive AZs and the surrounding AL. The AZs positive for ORCO-GFP were enriched for BRP in comparison to LN1-derived AZs using either GFP fusion protein; significance tests were carried out using Mann-Whitney U tests. BRP-short-GFP: $p = 0.0000265$, mCD8-GFP: $p = 0.00179$. No significant difference was observed between BRP-short-GFP- and mCD8-GFP-based ratios: ORCO-GAL4: $p = 0.189$, LN1-GAL4: $p = 0.0595$. The Bonferroni-corrected significance threshold was $\alpha = 0.05/4 = 0.0125$.

Graphs show medians, interquartile ranges, and min/max values.

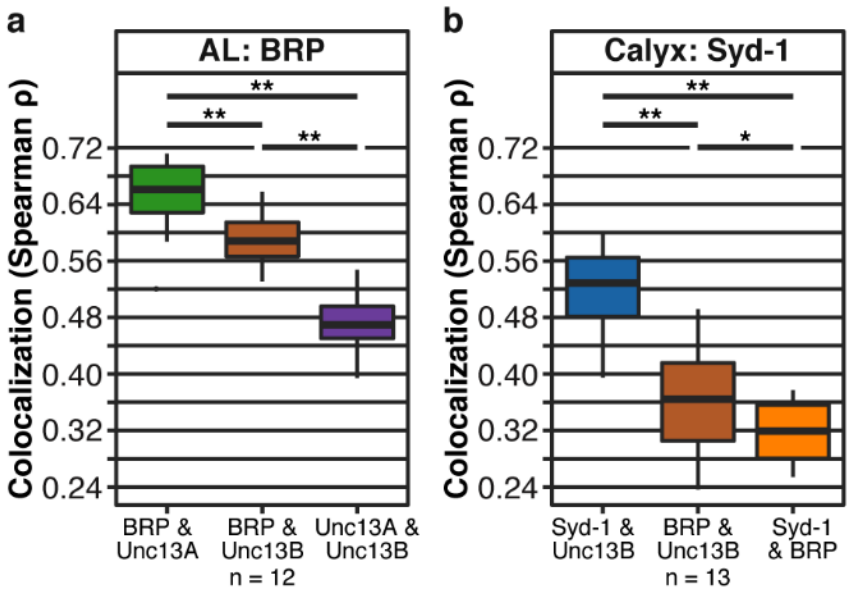

Figure S2: Colocalization analysis of the scaffold proteins BRP/Syd-1 and the Unc13 isoforms Unc13A/Unc13B, related to Figure 1 and Figure 2

Colocalization analysis using the Fiji Coloc 2 plugin (Spearman correlation) was conducted to examine pixel intensity correlations over space in single confocal images. We analyzed two separate sets of triple stainings, based on the available antibody combinations. All significance tests were carried out using the paired Wilcoxon signed-rank test. The Bonferroni-corrected significance threshold was $\alpha = 0.05/3 = 0.0167$ for each staining group. Sample sizes (n) are indicated at the bottom of the plots.

(a) BRP^{Nc82}, Unc13A, Unc13B triple staining analyzed in the AL where BRP^{Nc82} showed a heterogeneous distribution. The colocalization of BRP^{Nc82} and Unc13A was significantly higher than the colocalization of either BRP^{Nc82} and Unc13B ($p = 0.00049$) or Unc13A and Unc13B ($p = 0.00049$); the colocalization of BRP^{Nc82} and Unc13B was significantly higher than the one of Unc13A and Unc13B ($p = 0.00049$).

(b) Syd-1, BRP^{Nc82}, Unc13B triple staining analyzed in the calyx where Syd-1 showed a heterogeneous distribution. The colocalization of Syd-1 and Unc13B was significantly higher than the colocalization of either BRP^{Nc82} and Unc13B ($p = 0.00024$) or Syd-1 and BRP^{Nc82} ($p = 0.00024$); the colocalization of BRP^{Nc82} and Unc13B was significantly higher than the one of Syd-1 and BRP^{Nc82} ($p = 0.0017$).

Graphs show medians, interquartile ranges, and min/max values.

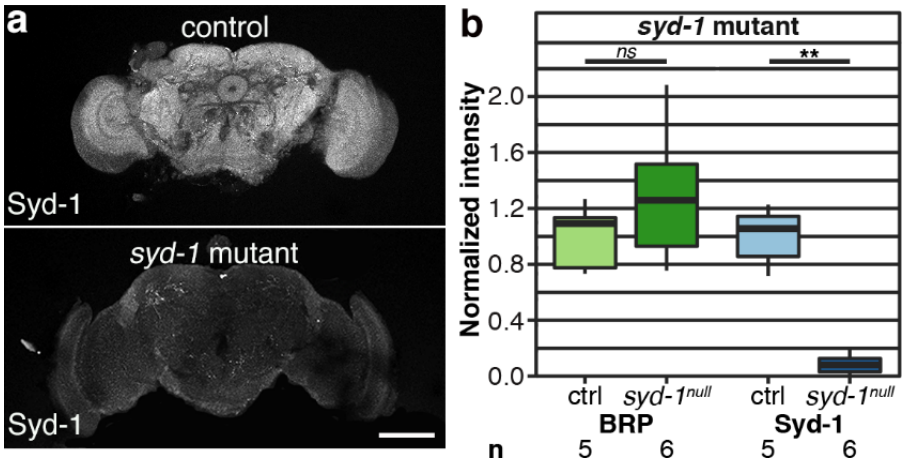

Figure S3: Quantification of the antibody staining reduction in *syd-1* null mutants in the adult *Drosophila* brain, related to Figure 3

(a) Confocal images of *Drosophila* central brains of *syd-1* mutant flies (*syd-1*$^{ex1.2}$/*syd-1*$^{ex3.4}$) in comparison to *w*^{1118} controls, stained against Syd-1; scale bar: 100 μm.

(b) Analysis of average staining intensities of BRP^{Nc82} and Syd-1 in *syd-1* mutants normalized to controls (ctrl). Average intensity levels of Syd-1 were significantly downregulated to 8.7 % of control levels ($p = 0.0013$). BRP^{Nc82} levels were not altered ($p = 0.25$). Association tests were conducted using a permutation test (10,000 permutations), based on linear mixed models with the imaging batch as a random effect. The permutation test was carried out because the residuals of the regression were not normally distributed. The Bonferroni-corrected significance threshold was $\alpha = 0.025$. Sample sizes (n) are indicated at the bottom of the plots. The graph shows medians, interquartile ranges, and min/max values.

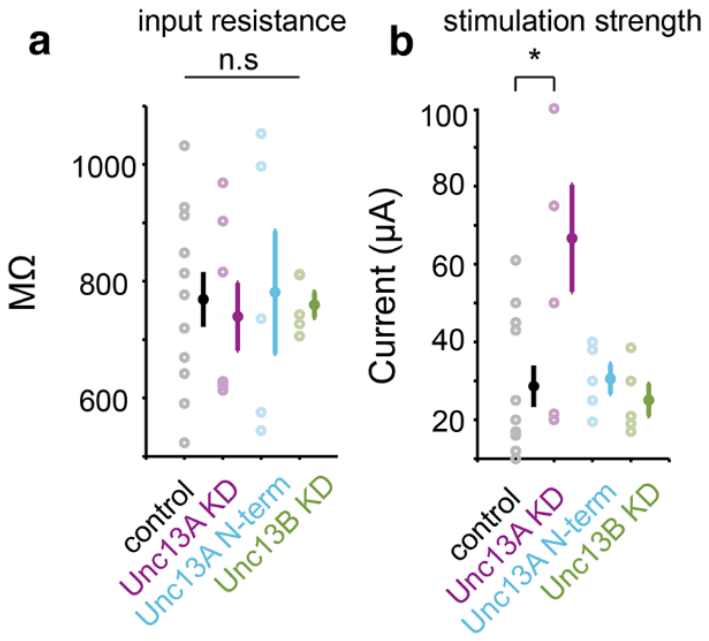

Figure S4: PN input resistances are similar across control and *unc13A/B* KD flies, related to Fig. 5
(a) Input resistance.
(b) Stimulation current at the antennal nerve necessary to evoke EPSCs at the downstream PNs. *unc13A* KD: pb-GAL4>UAS-*unc13A*-RNAi-A1; *unc13B* KD: pb-GAL4>UAS-*unc13B*-RNAi-B3; *unc13A* N-term: pb-GAL4>UAS-*unc13A-N-term-GFP*. An increased current was required to elicit responses in the *unc13A* KD flies compared to controls ($p < 0.01$; unpaired Student's t-test). Mean values ± SEM are represented.

.

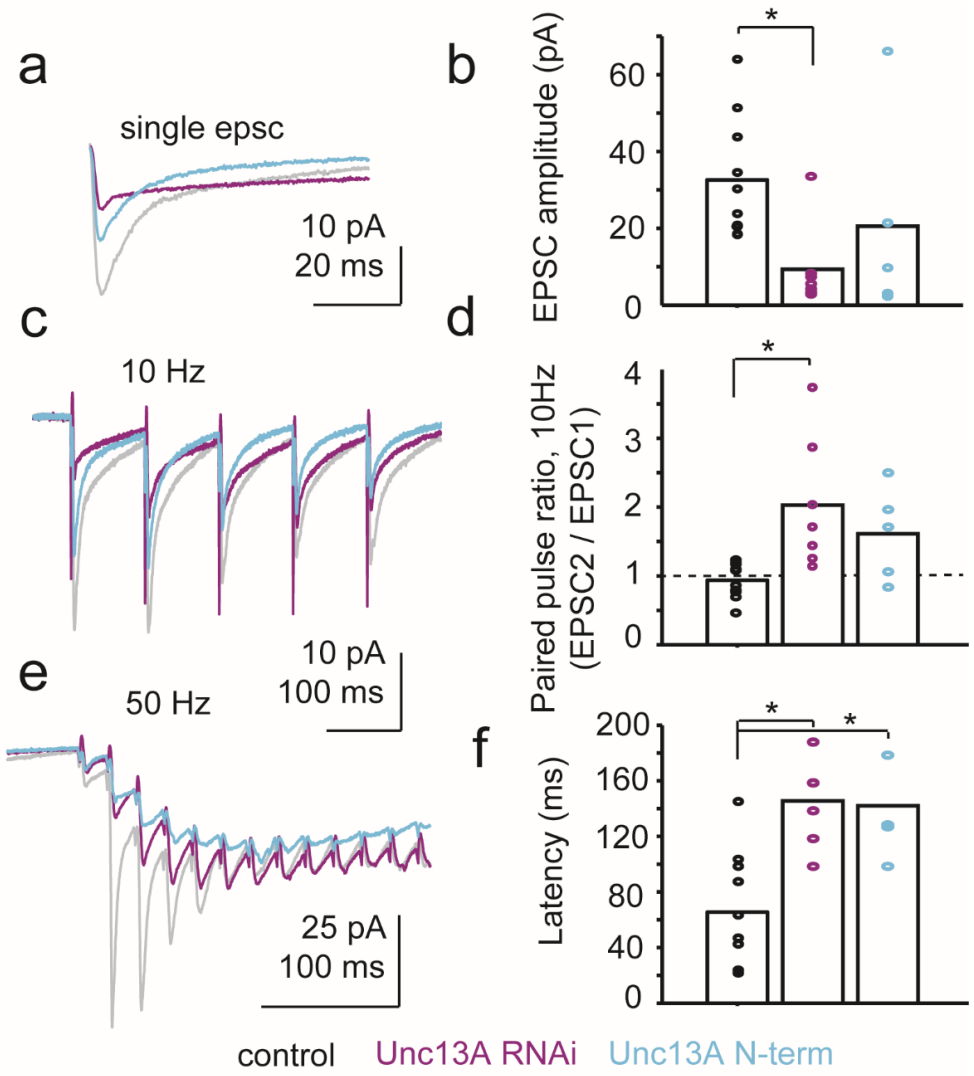

Figure S5: Loss of Unc13A by either RNAi-mediated knockdown or overexpression of a dominant-negative construct produces similar effects at the ORN-PN synapse, related to Figure 5
(a) Group-averaged single EPSCs; control (n = 10 cells), *unc13A* KD (n = 7 cells), *unc13A* dominant negative (DN, n = 5 cells). **(b)** Quantification of EPSC amplitudes across genotypes. EPSC amplitudes differed between genotypes ($F = 3.71$, $p < 0.05$, one-way ANOVA with Tukey post-hoc comparison). EPSCs were significantly smaller in *unc13A* KD flies compared to controls ($p < 0.01$, unpaired Student's t-test). **(c)** Group-averaged EPSCs evoked by 10 Hz stimulation; control (n = 10 cells), *unc13A* KD (n = 7 cells), *unc13A* DN (n = 5 cells). **(d)** Quantification of the paired-pulse ratio (PPR) between first and second EPSCs across genotypes. PPRs were different between genotypes ($F = 6.16$, $p < 0.01$, one-way ANOVA with Tukey post-hoc comparison). EPSCs were significantly smaller in *unc13A* KD flies compared to controls ($p < 0.01$, unpaired Student's t-test). **(e)** Group-averaged EPSCs evoked by 50 Hz stimulation; control (n = 10 cells), *unc13A* KD (n = 7 cells), *unc13A* DN (n = 5 cells). **(f)** Quantification of latency to peak current evoked by 50 Hz stimulation across genotypes. The latency, which was quantified as the time between the onset of 50 Hz stimulation and the peak evoked current, differed between genotypes ($F = 12.29$, $p < 0.001$, one-way ANOVA with Tukey post-hoc comparison). The latency was increased in *unc13A* KD flies ($p < 0.001$, unpaired Student's t-test) and *unc13A* DN flies ($p < 0.01$, unpaired Student's t-test) as compared to controls. In **(a)**, **(c)**, and **(e)**, stimulus artifacts were minimized for clarity of presentation by linearly extrapolating between the pre- and post-stimulation artifact periods in Figure 5. Bar charts represent mean values.

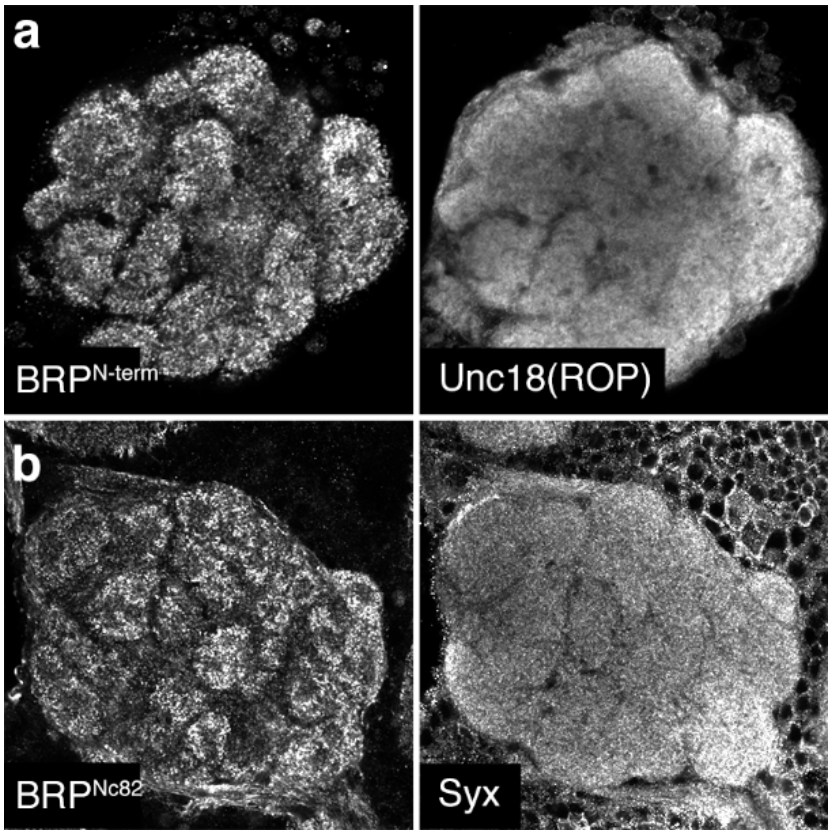

Figure S6: Distribution of the release factors Syntaxin (Syx) and Unc18 (ROP) in the AL, related to Figure 1
(a, b) Confocal sections of adult w^{1118} ALs.
(a) BRP N-term (left) and Unc18 (ROP) (right).
(b) BRP C-term (Nc82) (left) and Syntaxin (Syx) (right).

Supplemental Experimental Procedures

Resource Table

REAGENT or RESOURCE	SOURCE	IDENTIFIER
Antibodies		
Mouse monoclonal BRP^{Nc82}	DSHB; Wagh et al., 2006	Cat# nc82, RRID: AB_2314865
Guinea Pig Unc13A$^{N\text{-}term}$	Böhme et al., 2016	N/A
Rabbit Unc13B$^{N\text{-}term}$	Böhme et al., 2016	N/A
Guinea Pig Unc13B$^{N\text{-}term}$	This paper, self-raised	N/A
Rabbit Syd-1	Owald et al., 2010	N/A
Mouse ROP (Unc18)	DSHB	Cat# DSHB 4F8
Mouse Syntaxin	DSHB	Cat# DSHB 8C3
Chicken GFP	Abcam	Cat# ab13970
Rabbit BRP$^{N\text{-}term}$	Fouquet et al., 2009	N/A
Goat anti Mouse IgGs Alexa Fluor 488	Invitrogen	Cat# A21467
Goat anti Mouse IgGs Cy3	Abcam	Cat# ab102370
Goat anti Mouse IgGs Star635P	Abberior	Cat# 2-0002-007-5
Goat anti Rabbit IgGs Cy5	Invitrogen	Cat# A10523
Goat anti Rabbit IgGs Alexa Fluor 594	Invitrogen	Cat# A11037
Goat anti Guinea Pig IgGs Alexa Fluor 594	Invitrogen	Cat# A11076
Goat anti Chicken IgGs Alexa Fluor 488	Invitrogen	Cat# A21467
FluoTag X4 anti GFP Star635P	NanoTag Biotechnologies	Cat# N0304-Ab635P-L
Experimental Models: Organisms/Strains		
Drosophila: w^{1118} (control)	Hazelrigg et al., 1984	N/A
Drosophila: elav-GAL4 (X chromosome)	Lin and Goodman, 1994	N/A
Drosophila: MB247-GAL4	Zars et al., 2000	N/A
Drosophila: OR83b-GAL4 (ORCO-GAL4)	Wang et al., 2003	
Drosophila: GH146-GAL4	Bloomington	Cat# stock 30026
Drosophila: GMR-GAL4	Yamada et al., 2003	N/A
Drosophila: LN1^{NP1227}-GAL4	Das et al., 2008	N/A
Drosophila: mz19-GAL4	Ito et al., 1998	N/A
Drosophila: 17D-GAL4	Melzig et al., 1998	N/A
Drosophila: Pebbled-GAL4 (Pb-GAL4)	Nagel lab, NYU Sweeney et al., 2007	N/A
Drosophila: NP3056-GAL4,mCD8-GFP	Nagel lab, NYU	N/A
Drosophila: UAS-10xmCD8-GFP	Janelia Farm	N/A
Drosophila: UAS-brp-RNAi-B3,C8	Wagh et al., 2006	N/A
Drosophila: UAS-unc13A-RNAi-A1	This paper	N/A
Drosophila: UAS-unc13B-RNAi-B3	This paper	N/A
Drosophila: UAS-Cac-GFP	Liu et al., 2011	N/A
Drosophila: UAS-Brp^{short}-GFP	Christiansen et al., 2011	N/A
Drosophila: UAS-Unc13A^{Nterm}-GFP	Reddy-Alla et al., 2017	N/A
Drosophila: Syd-1 $^{ex1.2}$/Syd-1 $^{ex3.4}$	Owald et al., 2010	N/A
Drosophila: EMS7.5/P84200	Böhme et al., 2016	N/A
Drosophila: Del100BPacman/Del100BPacman; P84200/P84200	Böhme et al., 2016	N/A

Drosophila: Unc13Pacman/Unc13Pacman; P84200/P84200	Böhme et al., 2016	N/A
Drosophila: UAS-ChR2	Nagel lab, NYU	N/A
Oligonucleotides		
Unc13_B3-R: AATTCGCGATCCAACAAACTATCTTGATTATGCTTG AATATAACTAATCAAGATAGTTTGTTGGATCACTG	This paper	N/A
Unc13_B3-F: CTAGCAGTGATCCAACAAACTATCTTGATTAGTTAT ATTCAAGCATAATCAAGATAGTTTGTTGGATCGCG	This paper	N/A
Unc13_A1-R:AATTCGCGGGTTAGGACATAATAATCTATATGCT TGAATATAACTATAGATTATTATGTCCTAACCCACT G	This paper	N/A
Unc13_A1-F: CTAGCAGTGGGTTAGGACATAATAATCTATAGTTA TATTCAAGCATATAGATTATTATGTCCTAACCCGCG	This paper	N/A
Unc13-IsoA-Nterm-Rev 5'- ATTAAGCTGCATGATTATTTTATTG-3'	This paper	N/A
Unc13-IsoA-Nterm-FW 5'- CACCATGACGCACTACGTGAGGC -3'	This paper	N/A
Software and Algorithms		
Amira	FEI	6.0.0
AutoQuant	MediaCybernetics	X2.2.2
Leica LAS X Software	Leica Microsystems	http://www.leica-microsystems.com/home/
Huygens	SVI	https://svi.nl/HomePage
ImageJ	NIH	1.51j
MATLAB	MathWorks	R2011a
R	R Foundation	3.3.3
SPSS Statistics	IBM	v20
Custom ImageJ plugins and R scripts	This paper	http://ratios.andlauer.net
Other		
TCS SP8 confocal microscope	Leica Microsystems	http://www.leica-microsystems.com
TCS SP8 gSTED 3x microscope	Leica Microsystems	http://www.leica-microsystems.com

Contact for reagent and resource sharing

Further information and requests for resources and reagents should be directed to and will be fulfilled by the lead contact, Stephan J. Sigrist (stephan.sigrist@fu-berlin.de).

Animal rearing and fly strains
Fly strains were reared under standard laboratory conditions (Sigrist et al., 2003) at 25 °C, 65-70% humidity and constant 12/12 hours light/dark cycle in incubators. The food recipe is based on the current Bloomington recipe for *Drosophila* medium (BDSC, 2017). If not stated differently, 4-7d female flies were used for the experiments.

Overview of the fly stocks used in this paper: w^{1118} (Hazelrigg et al., 1984), *elav-GAL4 (Lin and Goodman, 1994)*, *OR83b-GAL4* (*ORCO-GAL4*) (Wang et al., 2003), LN1-GAL4 (NP1227-GAL4) (Das et al., 2008), Mz19-GAL4 (Ito et al., 1998), 17D-GAL4 (Melzig et al., 1998), Pebbled-GAL4 (Pb-GAL4) (Sweeney et al., 2007), UAS-brp-RNAi-B3, UAS-brp-RNAi-C8 (Wagh et al., 2006), UAS-Cac^{GFP} (Liu et al., 2011), UAS-Brp^{short}-GFP (Christiansen et al., 2011), UAS-$Unc13A^{Nterm}$-GFP (Reddy-Alla et al., 2017), Syd-$1^{1.2}$/Syd-$1^{3.4}$ (Owald et al., 2010), EMS7.5/P84200 (Böhme et al., 2016), *Del100BPacman/Del100BPacman*; $Unc13^{P84200}$/$Unc13^{P84200}$ (Böhme et al., 2016), *Unc13Pacman/Unc13Pacman*; $Unc13^{P84200}$/$Unc13^{P84200}$ (Böhme et al., 2016). The $Unc13^{P84200}$ stock was obtained from Kyoto DGGR #101911. UAS-unc13A-RNAi-A1 and UAS-unc13B-RNAi-B3 are first published in this paper.

Experiment specific genotypes: If not stated otherwise, the strain used for general observations was w^{1118}. Genotypes used for deletions: $Unc13A^{null}$: $Unc13A^{EMS7.5}$/$Unc13^{P84200}$; $Unc13B^{null}$: *Del100BPacman/+;* $Unc13^{P84200}$/$Unc13^{P84200}$. Syd^{null}: $Syd^{ex1.2}$/$Syd^{ex3.4}$. Controls for all mutants: w^{1118}. Genotypes for knockdowns: Brp^{RNAi}*: elav-GAL4/+; UAS-brp-RNAi-B3,UAS-brp-RNAi-C8/+*. Controls: elav-GAL4/+; w^{1118}. Genotypes used for ratio experiments: *ORCO-GAL4/+; UAS-*Brp^{short}*-GFP/+. LN1-GAL4/+; UAS-*Brp^{short}*-GFP/+. Mz19-GAL4/+; UAS-*Brp^{short}*-GFP/+. 17D-GAL4/+; UAS-*Brp^{short}*-GFP/+. ORN-driven UAS-Cac-GFP: pb-GAL4/+; UAS-Cac-GFP/+*. Genotypes used for electrophysiology: *pb-GAL4/+; UAS-unc13A-RNAi-A1/+. pb-GAL4/+; UAS-unc13B-RNAi-B3/+. pb-GAL4/+; UAS-Unc13-Nterm-GFP. UAS-Unc13-Nterm-GFP, UAS-ChR2/+;NP3056-GAL4,UAS-mCD8-GFP/ UAS-unc13B-RNAi-B3. UAS-ChR2/+;NP3056-GAL4,UAS-mCD8-GFP/ UAS-unc13A-RNAi-A1. UAS-ChR2/+;NP3056-GAL4,UAS-mCD8-GFP/ +* (Control).

RNA interference
unc13 RNAi constructs were designed and cloned into *pWalium20* vectors, following the TRIP protocol from Harvard Medical School (Harvard medical school, 2017). Constructs were injected into *VK27 TM3(sb)* flies (Bloomington *Drosophila* stock center stock 9744) by BestGene (BestGene, Inc, Chino Hills, USA). The following primers were used:
Unc13-B3-Reverse:
AATTCGCGATCCAACAAACTATCTTGATTATGCTTGAATATAACTAATCAAGATAGTTTGTTGGATCACTG.
Unc13-B3-Forward:
CTAGCAGTGATCCAACAAACTATCTTGATTAGTTATATTCAAGCATAATCAAGATAGTTTGTTGGATCGCG.
Unc13-A1-Reverse:
AATTCGCGGGTTAGGACATAATAATCTATATGCTTGAATATAACTATAGATTATTATGTCCTAACCCACTG.
Unc13-A1-Forward:
CTAGCAGTGGGTTAGGACATAATAATCTATAGTTATATTCAAGCATATAGATTATTATGTCCTAACCCGCG.

Immunohistochemistry
Unless stated differently, 4-7d female fruit flies were used for the experiments. For *brp* knockdown experiments, 4-7d males raised on 29°C were utilized to boost RNAi efficacy.
The standard immunohistochemistry protocol illustrated below was slightly adjusted within the different experimental settings. Adult brains were dissected in ice-cold (HL3) solution, fixed for 40 min in 4% paraformaldehyde (PFA) in 1x phosphate-buffered saline (PBS), pH 7.2, at room temperature (RT), washed with 0.6 % Triton X-100 in 1x PBS (PBT) and blocked in 10% normal goat serum (NGS) in 0.6% PBT for 2 hrs at RT. The brains were incubated with primary antibodies together with 5% NGS in 0.6%

PBT for 48 hours at 4°C and then washed in 0.6% PBT for 3 hrs. (6x 30min after rinsing), followed by overnight incubation with secondary antibodies at 4°C. The brains were then washed for 3 hrs with 0.6% PBT and mounted in VectaShield (Vector Laboratories, Burlingame, USA) on glass slides. STED samples were mounted in ProLong® Gold Antifade Mountant (Invitrogen, Carlsbad, USA) with high precision cover slips No. 1.5H (Carl Roth GmbH & Co. KG, Karlsruhe, Germany).

Image acquisition

Conventional confocal images were acquired at constant 21°C with TCS SP8 confocal microscopes (Leica Microsystems, Wetzlar, Germany) using either a 63×, 1.4 NA oil or a 63×, 1.3 NA glycerin objective for detailed scans. For whole brain scans, either a 20×, 0.7 NA or a 40x, 1.3NA oil objective were used. The lateral pixel size was set to values around 100 nm for detailed scans. Typically, 1024 × 1024 pixel resolution images were scanned at 400 Hz using 3× line averaging for stacks, with lower scan speed and higher average for detailed single images. All images were acquired using the Leica LAS-X software. Deconvolution of images was conducted using AutoQuant X2.2.2 (MediaCybernetics, Rockville, USA). Confocal stacks were processed using ImageJ 1.51j (Schindelin et al., 2012a; Schneider et al., 2012). Contrast was adapted for visualization only, where necessary, using either the levels tool in Adobe Photoshop CC 2017.0.1 (Adobe, San José, USA) or ImageJ. Images shown in a comparative figure were processed with exactly the same parameters. Images were not post-processed before quantification, but exclusively afterwards and only for visualization.

STED microscopy was performed using a Leica Microsystems TCS SP8 gSTED 3x setup equipped with a pulsed white light laser (WLL; ~80-ps pulse width, 80-MHz repetition rate; NKT Photonics) and two STED lasers for depletion (continuous wave at 592 nm, pulsed at 775 nm). The pulsed 775 nm STED laser was triggered by the WLL. Images were acquired with a 100×, 1.4 NA oil immersion objective. 1024 × 1024 pixel resolution 2D STED images were scanned at 600 Hz using 8× line averaging. The lateral pixel size was set to values of ~20 nm, stacks of three images each were acquired, with a step size of 130 nm for a better estimation of the point spread function (PSF). To minimize thermal drift, the microscope was housed in a heatable incubation chamber. STED images were processed using the Huygens deconvolution software (SVI, Hilversum, The Netherlands) using a theoretical PSF automatically computed, based on a pulsed STED-optimized function and the specific microscope parameters. Default deconvolution settings were applied.

Quantification of average label intensities

Images were acquired as described above. For each dataset, fruit flies of different genotypes were dissected, treated, and processed equally and images were acquired with the same microscope/laser setting within the same scan session, alternating between different genotype groups to keep the conditions comparable. If a genotype comparison consisted of more than one dataset, values were normalized to the respective control group. Raw images were not altered or further processed prior to analysis. Average fluorophore intensities were analyzed using Amira 6.0.0 (FEI, Hillsboro, USA). Regions of interest (ROIs) were selected within the three-dimensional image stack using the Amira tool *Segmentation Editor*. The labels were optimized for all three fluorophore channels, excluding artifacts and non-neuropil staining. Mean intensity values within the 3D mask were calculated using the *Material Statistics* tool for all three channels. For background correction, mean intensities in non-neuropil regions (3D labels selected in the Brp^{NC82} channel) were subtracted from each individual neuropil value.

Background-corrected knockdown and deletion data were analyzed in *R* 3.3.3 with linear mixed models using the function *lmer* in the *R* package *lme4* (Bates et al., 2015). Animals were typically stained and imaged in several batches and 1-2 hemispheres per animal were scanned. Association of genotype with antibody levels was therefore tested using imaging batch and animal as nested random effects. In cases were the residuals of the model were not normally distributed (assessed via Shapiro-Wilk tests), the association was confirmed using a non-parametric permutation test using 10,000 permutations. If the permutation tests confirmed the results, the permutation test was not further mentioned in the text or figure legends. In case of deviations potentially influencing the significance level, the permutation test result is indicated. For the scaffold protein reduction experiment (Fig. 3), association tests were conducted using

linear mixed models with imaging batch and animal as nested random effects. A Bonferroni-corrected significance threshold of $\alpha = 0.0167$ was used for the *brp* KD and the *syd-1* deletion, and $\alpha = 0.025$ for the *unc13A/B* deletions.

STED distance analysis

GFP-labeled calcium channels (UAS-Cac-GFP) (Liu et al., 2011) were expressed in olfactory receptor neurons (ORNs) using the pb-GAL4 line (Sweeney et al., 2007). GFP-signals were enhanced using FluoTag®-X4 anti-GFP (NanoTag Biotechnologies GmbH, Göttingen, Germany) tagged with STAR 635p (Abberior, Göttingen, Germany). This fluorescent nanobody labels epitopes with a distance below 4 nm and each GFP is labeled with up to four fluorophores. GFP labels were combined with antibody stainings against either Unc13A or -B. All images within one dataset were acquired with the same microscope settings and deconvolved with Huygens (SVI, Hilversum, The Netherlands) using the same deconvolution parameters. Distances between fluorophores were analyzed using ImageJ 1.51j. STED channels for Cac-GFP and the respective Unc13 isoform were merged for each image (total size 19,39 × 19,39 μm). Twenty straight lines with a defined length of 400 nm were manually drawn through the centers of the signal from both channels in close proximity. Criteria for the selection of punctae were: Proximity closer than 400 nm, comparable relative intensity between the two channels, indicating the same Z position, and definite fluorophore spots. Lines were saved as regions of interests (ROIs). For analysis of peak-to-peak distances between the two fluorophore channels, the image-specific ROI sets were applied onto the STED channels and the 8-bit intensity values along the lines were detected using the *Fiji Multi-Plot* tool in the ROI manager. The distance between the intensity maxima of both channels was saved for each ROI as the distance for the respective analyzed AZ. The distances were analyzed using linear mixed models, as described above. Because several measurements were taken per image (scan), several images were scanned per hemisphere, and 1-2 hemispheres were analyzed per animal, scan, hemisphere, and animal were used as nested random effects.

Cluster distance and k nearest-neighbor analysis

For the cluster distance analysis, planar AZs were visually identified on deconvolved STED images of immunostainings against BRP^{NC82}. Several subregions of the image containing individual AZs were selected within 1 × 1 μm ROIs (53 × 53 pixels) in ImageJ v1.48v. The subregions were copied to new 1 μm^2 subimages for each channel. To identify the exact position of the AZ center, even smaller AZ ROIs were placed on the 1 μm^2 BRP^{NC82} subimages. AZ ROIs were rectangular, of variable size and chosen to be as small as possible yet at the same time to contain the full AZ as visible in the BRP signal. The starting positions $x_{AZ\text{-}ROI}$ and $y_{AZ\text{-}ROI}$ of each AZ ROI within the 1 μm^2 subimages was extracted using the *ImageJ* function *Roi.getBounds* and the AZ region within the AZ ROI was copied to a new image. The lowest intensity pixel was determined for each AZ region and its value subtracted from all pixel values in this image before the position of the AZ center was determined by calculating the coordinates ($x_{center\_of\_mass(AZ\text{-}image)}$ and $y_{center\_of\_mass(AZ\text{-}image)}$) of the center of mass, taking the pixel intensities into account and using output values XM and YM of the *ImageJ* function *Measure* (settings: mean min center redirect=None decimal=4). These coordinates identify the x and y position of the AZ center within the AZ ROI. To obtain the position of the AZ center in the context of the larger, 1 μm^2 subimages, the position of AZ ROIs within the 1 μm^2 ROI was taken into account ($x_{AZ\text{-}center(1\mu m^2\text{-}image)}=x_{center\_of\_mass(AZ\text{-}image)}+x_{AZ\text{-}ROI}$ and $y_{AZ\text{-}center(1\mu m^2\text{-}image)}=y_{center\_of\_mass(AZ\text{-}image)}+y_{AZ\text{-}ROI}$). To investigate the spatial relation of Unc13A or Unc13B to the AZ center, the same 1 μm^2 ROIs were used in the second channel as had been used for the first one. The position of protein spots was determined by first detecting local intensity maxima using the *ImageJ* function *Find maxima* (noise=5 output=[PointSelection]), followed by identifying their positions using the output values “X” and “Y” of the *ImageJ* function *Measure* (settings: “mean centroid center limit display redirect=None decimal=4”). Our procedure allowed reading out up to 50 such spots per AZ, but in reality, far fewer (roughly 20 in the case of Unc13A and of Unc13B) were detected.

Subsequently, the distance of protein spots to the AZ center was calculated using *Matlab* (v7.12.0.635 R2011a 64 bit, Mathworks, Natick, USA). The Euclidean distance of Unc13A and Unc13B spots to the center of mass of the BRP^{NC82} staining was determined. For each AZ, the observed distances were ranked and the minimum distance selected. Furthermore, the number of observed spots within distance bins from the BRP ring center (0-50 nm, 50-100 nm, 100-150 nm and 150-200 nm) was counted and

divided by the total number of either Unc13A or Unc13B spots found within a 200 nm radius. To obtain estimates for the entire brain, all values retrieved were averaged across all AZs per brain.
Statistical tests were conducted in SPSS (IBM, Armonk, USA). Normality of data was tested with the Shapiro-Wilk test and by inspection of histograms and QQ plots. The nonparametric Mann Whitney U test was used for analyses. Graphs show medians, interquartile ranges and min/max values and n indicates the number of animals tested.

Electrophysiology
Whole-cell patch-clamp recordings from PNs and LNs were made as described (Nagel et al., 2015; Nagel and Wilson, 2016). Female flies, 1-2 days post-eclosion, were positioned in a horizontal platform, with the dorsal part of the fly head above the platform and most of the fly below the platform. The dorsal part of the fly head was dissected to expose the brain and bathed in external saline containing 103 mM NaCl, 3 mM KCl, 5 mM TES, 8 mM trehalose, 10 mM glucose, 26 mM $NaHCO_3$, 1 mM NaH_2PO_4, 4 mM $MgCl_2$ and 1.5 mM $CaCl_2$. Cell bodies were visualized using infrared optics and a 40× water-immersion objective on an upright compound microscope (Olympus BX51). Patch pipettes (6-8 MΩ) were pulled the day of the recording and filled with internal solution containing 140 mM CsOH, 140 mM aspartic acid, 10 mM HEPES, 1 mM EGTA, 1 mM KCl, 4 mM MgATP, 0.5 mM Na_3GTP, 5 mM QX-314•Cl^- and 13 mM biocytin hydrazide. For current clamp recordings from presynaptic LNs KOH was used instead of CsPH. The pH of the internal solution was adjusted to 7.2 ± 0.1 and osmolarity to 265 ± 3 mOsm. PNs were identified by characteristic location and size within the antennal lobe. PNs with input resistance less than 500 MΩ or greater than 1200 MΩ were excluded from analysis, as were PNs in which an EPSC could not be elicited by 100 μA of current injection into the antennal nerve. To electrically stimulate presynaptic ORN axons, the antennae were removed and the ipsilateral antennal nerve was drawn into a large diameter pipette filled with saline. The nerve bundle was stimulated using a WPI stimulus isolator in constant current mode, with intensities ranging from 10 – 100 μA. The stimulus intensity was adjusted to the minimum amplitude that reliably elicited an EPSC on the first pulse. For LN recordings, channel rhodopsin was stimulated with 470 nm light through the microscope objective. We first made current clamp recordings from GFP+ LNs and adjusted light intensity so that robust spiking was obtained. The same intensity settings were used for GFP-LN recordings in voltage clamp. LNs were identified based on morphology and electrophysiological properties. After voltage clamp experiments, the identity of LNs was confirmed by switching briefly to current clamp mode and observing the waveforms of spontaneous spikes. Comparisons between groups were performed with a Kruskal-Wallis or one-way ANOVA test as indicated in the text. In the quantification of paired-pulse ratios (Figure 5), one *unc13B* KD recording was excluded from this analysis because no EPSC was produced in response to the first stimulation pulse.

Ratiometric analysis of presynaptic proteins
Ratios between two presynaptic antibody signal intensities were calculated for each pixel of three-channel, 8-bit, three-dimensional image stacks using custom *ImageJ* plugins (http://ratios.andlauer.net). First, the respective neuropil of interest (AL or calyx) was segmented from the rest of the brain using the *Fiji ImageJ* plugin *Segmentation Editor* (Christiansen et al., 2011; Schindelin et al., 2012b). A second mask was generated for GFP-positive voxels within the neuropil of interest. Second, we applied a percentile threshold to each image to remove unspecific background staining (non-AZ signal) from the masked regions. Voxels below the threshold were set to an intensity value of zero. For analysis of whole neuropils, the percentile threshold was 0.8, for the analysis of GFP-positive voxels 0.95. Because intensities vary within image stacks, each stack was divided into substacks for the determination of optimal absolute intensity value thresholds. Third, voxelwise ratio values were calculated. All oversaturated voxels (absolute intensity 255) were omitted from the calculation of ratio-based statistics. For visualization, ratios were ranked and mapped to a false-color gradient. This allowed for highlighting of synapse populations with especially strong differences in AZ protein intensity. Fourth, weighted median ratios were calculated on real (non-ranked) ratio values in *R* v3.3.3, once for the whole neuropil and once for the GFP-positive areas. For normalization, median ratios of GFP-positive voxels were divided by median ratios of the whole neuropil. Normalized median ratios were compared using Mann-Whitney U tests. The source code of all *ImageJ* plugins and the *R* scripts are available for download at http://ratios.andlauer.net.

Colocalization analysis
Colocalization analyses were conducted using the *Fiji Coloc 2* plugin (https://imagej.net/Coloc_2). The colocalizations between pairs of two antibodies in single image planes of triple stainings were analyzed using Spearman correlation. Spearman rank correlation coefficients were compared using the paired Wilcoxon signed-rank test.

Supplemental References

Bates, D., Mächler, M., Bolker, B., and Walker, S. (2015). Fitting Linear Mixed-Effects Models Using lme4. 2015 *67*, 48.

BDSC (2017). Bloom Food - Bloomington.

Böhme, M.A., Beis, C., Reddy-Alla, S., Reynolds, E., Mampell, M.M., Grasskamp, A.T., Lutzkendorf, J., Bergeron, D.D., Driller, J.H., Babikir, H.*, et al.* (2016). Active zone scaffolds differentially accumulate Unc13 isoforms to tune Ca(2+) channel-vesicle coupling. Nature neuroscience *19*, 1311-1320.

Christiansen, F., Zube, C., Andlauer, T.F., Wichmann, C., Fouquet, W., Owald, D., Mertel, S., Leiss, F., Tavosanis, G., Luna, A.J.*, et al.* (2011). Presynapses in Kenyon cell dendrites in the mushroom body calyx of Drosophila. J Neurosci *31*, 9696-9707.

Das, A., Sen, S., Lichtneckert, R., Okada, R., Ito, K., Rodrigues, V., and Reichert, H. (2008). Drosophila olfactory local interneurons and projection neurons derive from a common neuroblast lineage specified by the empty spiracles gene. Neural Dev *3*, 33.

Harvard medical school (2017). Cloning and sequencing.

Hazelrigg, T., Levis, R., and Rubin, G.M. (1984). Transformation of white locus DNA in Drosophila: Dosage compensation, zeste interaction, and position effects. Cell *36*, 469-481.

Ito, K., Suzuki, K., Estes, P., Ramaswami, M., Yamamoto, D., and Strausfeld, N.J. (1998). The organization of extrinsic neurons and their implications in the functional roles of the mushroom bodies in Drosophila melanogaster Meigen. Learn Mem *5*, 52-77.

Lin, D.M., and Goodman, C.S. (1994). Ectopic and increased expression of Fasciclin II alters motoneuron growth cone guidance. Neuron *13*, 507-523.

Liu, K.S., Siebert, M., Mertel, S., Knoche, E., Wegener, S., Wichmann, C., Matkovic, T., Muhammad, K., Depner, H., Mettke, C.*, et al.* (2011). RIM-binding protein, a central part of the active zone, is essential for neurotransmitter release. Science (New York, NY) *334*, 1565-1569.

Melzig, J., Rein, K.H., Schafer, U., Pfister, H., Jackle, H., Heisenberg, M., and Raabe, T. (1998). A protein related to p21-activated kinase (PAK) that is involved in neurogenesis in the Drosophila adult central nervous system. Curr Biol *8*, 1223-1226.

Nagel, K.I., Hong, E.J., and Wilson, R.I. (2015). Synaptic and circuit mechanisms promoting broadband transmission of olfactory stimulus dynamics. Nat Neurosci *18*, 56-65.

Nagel, K.I., and Wilson, R.I. (2016). Mechanisms Underlying Population Response Dynamics in Inhibitory Interneurons of the Drosophila Antennal Lobe. J Neurosci *36*, 4325-4338.

Owald, D., Fouquet, W., Schmidt, M., Wichmann, C., Mertel, S., Depner, H., Christiansen, F., Zube, C., Quentin, C., Korner, J.*, et al.* (2010). A Syd-1 homologue regulates pre- and postsynaptic maturation in Drosophila. J Cell Biol *188*, 565-579.

Reddy-Alla, S., Böhme, M.A., Reynolds, E., Beis, C., Grasskamp, A.T., Mampell, M.M., Maglione, M., Jusyte, M., Rey, U., Babikir, H.*, et al.* (2017). Stable Positioning of Unc13 Restricts Synaptic Vesicle Fusion to Defined Release Sites to Promote Synchronous Neurotransmission. Neuron *95*, 1350-1364.e1312.

Schindelin, J., Arganda-Carreras, I., Frise, E., Kaynig, V., Longair, M., Pietzsch, T., Preibisch, S., Rueden, C., Saalfeld, S., Schmid, B.*, et al.* (2012a). Fiji: an open-source platform for biological-image analysis. Nature Methods *9*, 676-682.

Schindelin, J., Arganda-Carreras, I., Frise, E., Kaynig, V., Longair, M., Pietzsch, T., Preibisch, S., Rueden, C., Saalfeld, S., Schmid, B.*, et al.* (2012b). Fiji: an open-source platform for biological-image analysis. Nat Methods *9*, 676-682.

Schneider, C.A., Rasband, W.S., and Eliceiri, K.W. (2012). NIH Image to ImageJ: 25 years of image analysis. Nature Methods *9*, 671-675.

Sigrist, S.J., Reiff, D.F., Thiel, P.R., Steinert, J.R., and Schuster, C.M. (2003). Experience-dependent strengthening of Drosophila neuromuscular junctions. J Neurosci *23*, 6546-6556.

Sweeney, L.B., Couto, A., Chou, Y.-H., Berdnik, D., Dickson, B.J., Luo, L., and Komiyama, T. (2007). Temporal Target Restriction of Olfactory Receptor Neurons by Semaphorin-1a/PlexinA-Mediated Axon-Axon Interactions. Neuron *53*, 185-200.

Wagh, D.A., Rasse, T.M., Asan, E., Hofbauer, A., Schwenkert, I., Durrbeck, H., Buchner, S., Dabauvalle, M.C., Schmidt, M., Qin, G.*, et al.* (2006). Bruchpilot, a protein with homology to ELKS/CAST, is required for structural integrity and function of synaptic active zones in Drosophila. Neuron *49*, 833-844.

Wang, J.W., Wong, A.M., Flores, J., Vosshall, L.B., and Axel, R. (2003). Two-photon calcium imaging reveals an odor-evoked map of activity in the fly brain. Cell *112*, 271-282.

Yamada, T., Okabe, M., and Hiromi, Y. (2003). EDL/MAE regulates EGF-mediated induction by antagonizing Ets transcription factor Pointed. Development *130*, 4085-4096.

Zars, T., Fischer, M., Schulz, R., and Heisenberg, M. (2000). Localization of a short-term memory in Drosophila. Science *288*, 672-675.